Soil Dynamics and Earthquake Engineering 147 (2021) 106798

Contents lists available at ScienceDirect

Soil Dynamics and Earthquake Engineering

journal homepage: www.elsevier.com/locate/soildyn

# Near-surface frequency-dependent nonlinear damping ratio observation of ground motions using SMART1

Chun-Hsiang Kuo [a,b,c], Jyun-Yan Huang [c,*], Che-Min Lin [c], Chun-Te Chen [d], Kuo-Liang Wen [a]

[a] Department of Earth Sciences, National Central University, No. 300, Zhongda Rd., Zhongli District, Taoyuan City, Taiwan, ROC
[b] Earthquake-Disaster & Risk Evaluation and Management Center, National Central University, No. 300, Zhongda Rd., Zhongli District, Taoyuan City, Taiwan, ROC
[c] National Center for Research on Earthquake Engineering, No. 200, Sec. 3, HsinHai Rd., Taipei City, Taiwan, ROC
[d] Institute of Earth Sciences, Academia Sinica, No. 128, Sec. 2, Academia Road, Nangang, Taipei City, Taiwan, ROC

ARTICLE INFO

*Keywords:*
Frequency-dependent damping
SMART1
Taiwan
Soil nonlinearity

ABSTRACT

The damping ratio is an important index used in soil nonlinearity studies and is mostly proportional to the shear strain increase. Previous researches indicated a frequency-independent damping in most cases. In this study, frequency-dependent damping was introduced from frequency-dependent $Q$ calculated through the spectral ratio method of near-surface structures using the power spectrum of strong motion records in the Strong Motion Array in Taiwan Phase I (SMART1). The dense SMART1 recorded significant strong motions in the 1980s, which can be used to identify soil nonlinearity at near surfaces. A 40%–50% increase in frequency-dependent damping for SMART1 was identified, with strain increasing from 0.01% to 0.1% in near-surface regions. A large damping was also found in the shallow sediments with mean Vs below 600 m/s on the topmost 500 m layers in the SMART1 database at a frequency range of 3–8 Hz, which is independent of the magnitude scaling or near-field travel distance scaling relations.

## 1. Introduction

Soil nonlinearity in site effects mostly result in a decrease in site resonance frequency and de-amplification at high frequencies (e.g., peak ground acceleration [PGA]). The former implies a reduction in the shear wave velocity induced from a material disturbance in shallow sub-layers during seismic wave propagation, whereas the latter is characterized with the increase in the damping ratio and the occurrence of a large strain in shallow subsurface sedimentary layers, particularly in alluvium sites [1–4]. Two important aspects have been introduced to understand soil nonlinearity behaviors, namely, seismology and geotechnical lab experiments. From a seismological point of view, de-amplification is identified through the observation of intensity in the time frequency domains (i.e., PGA, Fourier amplitude spectrum, spectral acceleration [SA]), which is commonly not followed in general site amplification. Considerable evidence on site effects that used the spectral ratio method, horizontal-to-vertical spectral ratio method (HVSR), and intensity ratios of observation station pairs or from observation to synthetic motions has been found by previous studies (methodologies were mainly referenced from Refs. [5–10]). For instance, Boore et al. indicated that de-amplification occurred in some soil sites after the 1989 Loma Prieta earthquake, which caused a nonlinear PGA attenuation relationship [2]. The site amplification factor becomes nonlinear relation from weak to strong motion in a specific frequency band where the strong motion would be reduced. Jarpe et al. identified a frequency-dependent de-amplification phenomenon in the low frequency band by comparing records of the main shock and aftershocks from a set of soil-to-rock station pairs [11]. Darragh and Shakal found more clear evidence within a wider frequency band from the soil-to-rock spectral ratio method by comparing the high-intensity main shock and aftershocks of the Loma Prieta earthquake [3]. Meanwhile, apparent soil nonlinearity effects were found by comparing observations and a ground motion simulation in linear site responses (i.e., stochastic point source simulation [6,12]) within a short distance from the epicenter, indicating the difficulty of extracting the phenomenon in seismological observations [7,13].

From the 1980s to the 1990s, three large-scale strong motion networks were installed in Eastern Taiwan, namely, the Lotung Large-Scale Seismic Test (LLSST), Strong Motion Array in Taiwan Phase I (SMART1), and SMART Phase II (SMART2), which recorded several high-intensity

* Corresponding author.
*E-mail addresses:* chkuo@ncu.edu.tw (C.-H. Kuo), jyhuang@narlabs.org.tw (J.-Y. Huang), cmlin@narlabs.org.tw (C.-M. Lin), pokayoke@earth.sinica.edu.tw (C.-T. Chen), wenkl@cc.ncu.edu.tw (K.-L. Wen).

https://doi.org/10.1016/j.soildyn.2021.106798
Received 20 November 2020; Received in revised form 28 March 2021; Accepted 25 April 2021
Available online 15 May 2021

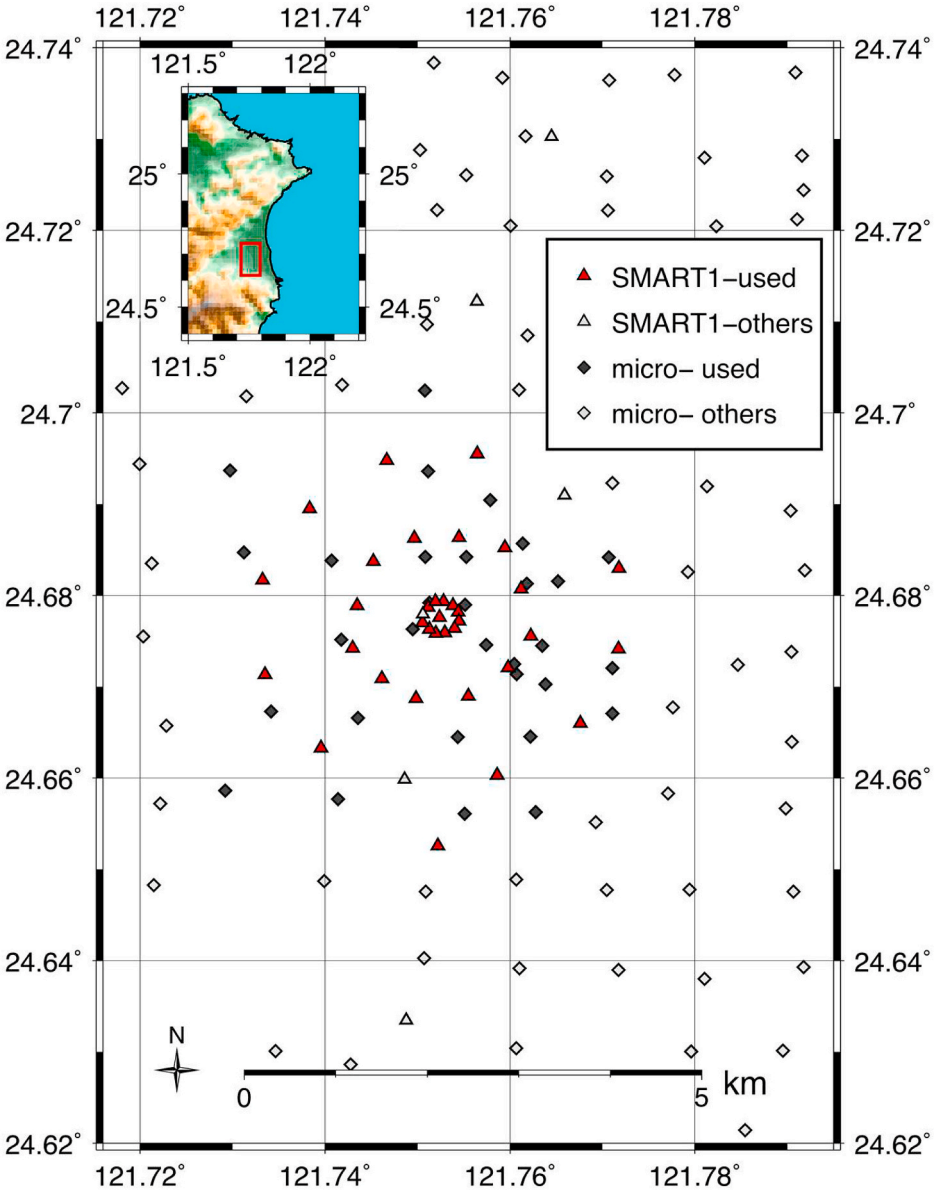


**Fig. 1.** Distribution of strong motion stations in SMART1 array and microtremor measurement points beneath SMART1. Red triangles and dark-gray diamonds represent stations used in this study, light-gray triangles are the SMART1 stations eliminated in this study due to useable data less than 10 events, light-gray diamonds are other microtremor measurements, and red rectangle is the location showed in this figure. (For interpretation of the references to color in this figure legend, the reader is referred to the Web version of this article.)

seismograms in alluvium sites [14–17] and provided worldwide opportunities for studying soil nonlinearities. Ratios of soil (i.e., surfaces or soft sites) to reference rock (downholes or stiff sites) motions of the LLSST, SMART1, and SMART2 indicated a drop in the PGA amplification factor, a de-amplification around the site effect-related frequency band, an effective shear wave velocity drop to around half with a PGA greater than 150 gal, and a shift in the resonance frequency behavior (site dominant frequency) to a lower frequency [18–24], mostly owing to the soil nonlinearity effect. Furthermore, a drop in the shear wave velocity was found in the seismic records of Port Island from the velocity inversion during the 1995 Kobe earthquake. This resulted in a time variety/recovery process of the shear wave-related property and permanent change owing to the occurrence of liquefaction [1]. Moreover, HVSR was introduced to identify the soil nonlinearities in the strong motions recorded in the LLSST and Port Island. The drop in the dominant frequency and de-amplification in the high-frequency spectrum were examined. The introduced HVSR-based method brings wide application possibilities because it is hard to find a good reference rock site, but it is easy to obtain the HVSR of strong motion stations in many regions [4]. Several follow-up studies have applied the HVSR technique to identify the occurrence of soil nonlinearities after earthquakes [25–33]. More recently, the quantitative identification of soil nonlinearities from seismic waves has received considerable attention, and several useful methods have been published, including the degree of nonlinearity (DNL) [34,35], percentage of nonlinearity [36], initiated frequency of nonlinearity [36], and the ratio of the dominant frequency of weak and strong motions [37]. Related applications will help us to understand the level of strong soil nonlinearity occurred in many cases [27,31,32,37–40].

Moreover, in geotechnical engineering, the characteristics of soil mechanics are different while dynamic loading (i.e., strong ground motions) occurred, where the soil displays linearity/elasticity under small stress and nonlinearity/elastoplasticity under large stress. The resulting experimental soil sample during a cyclic triaxial test indicated a hysteresis loop relation between the shear stress and shear strain. The shape of the initial loading curve was a hyperbola and a proportional relation between the shear stress and shear modulus was found [41–43]. Meanwhile, the basic shear stress-strain relation can be imagined as an ellipse loop in which the area of the hysteresis loop represents the energy loss of each stress-strain cycle and corresponds to hysteretic damping, which means that the dynamic loading process can be simply represented from the relations of the shear modulus and damping [44].

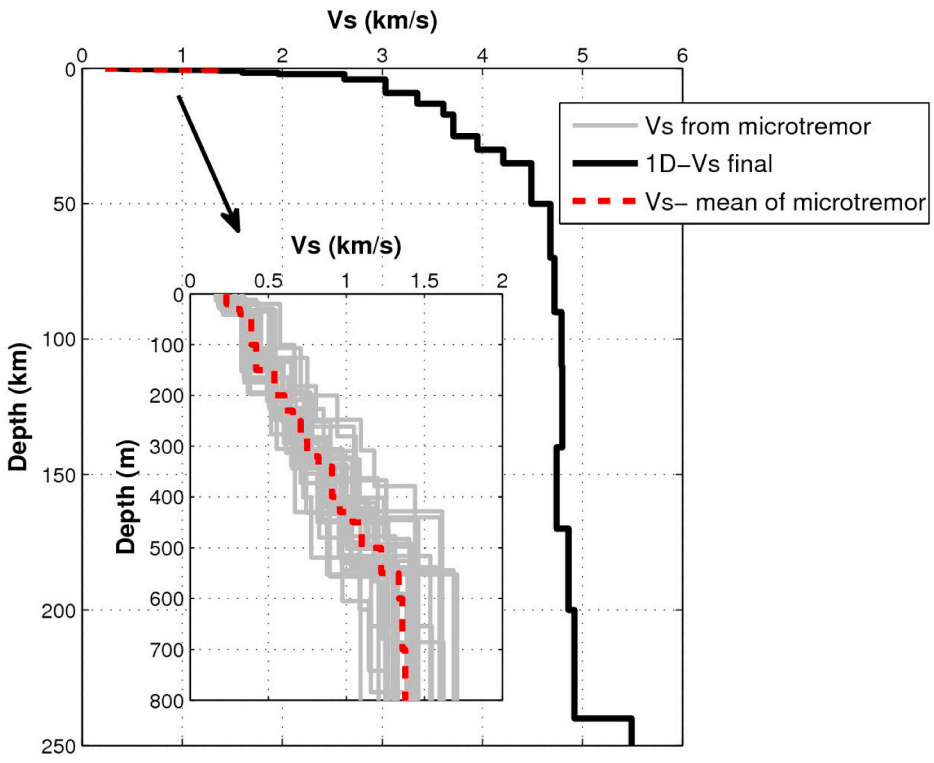


**Fig. 2.** 1D shear wave velocity structure used in the ray tracing technique from combining the CWB 1D structure for the deeper part and those inverted from MHVSR for the shallow part. Gray lines are from the 31 microtremor measurements near SMART1, red dash line is the mean structure, and the black line is the final model. (For interpretation of the references to color in this figure legend, the reader is referred to the Web version of this article.)

**Table 1**
1D velocity structure used in the ray tracing technique.

| Depth | Vs | Depth | Vs | Depth | Vs | Depth | Vs |
|---|---|---|---|---|---|---|---|
| 0.02 | 0.23 | 0.34 | 0.82 | 2 | 1.96 | 90 | 4.72 |
| 0.03 | 0.27 | 0.4 | 0.91 | 4 | 2.62 | 110 | 4.79 |
| 0.04 | 0.32 | 0.43 | 0.96 | 9 | 3.03 | 140 | 4.8 |
| 0.1 | 0.39 | 0.45 | 1.04 | 13 | 3.35 | 170 | 4.74 |
| 0.15 | 0.42 | 0.5 | 1.1 | 17 | 3.61 | 200 | 4.86 |
| 0.2 | 0.54 | 0.55 | 1.22 | 25 | 3.71 | 240 | 4.92 |
| 0.23 | 0.6 | 0.6 | 1.34 | 30 | 3.95 | 280 | 5.49 |
| 0.25 | 0.66 | 0.7 | 1.36 | 35 | 4.21 | | |
| 0.28 | 0.71 | 0.8 | 1.38 | 50 | 4.49 | | |
| 0.32 | 0.75 | 1.5 | 1.6 | 70 | 4.68 | | |

*Depth unit is in km, and Vs is in km/s.

Furthermore, if the constitutive relation of the stress-strain curve followed the abovementioned hysteresis loop, it would respond with the increasing damping ratio, and the shear strain would increase and result in a high-frequency de-amplification in seismological observations [21]. In addition, time-varying nonlinear hysteretic stress-strain relations with the depth and temporal changes of soil behaviors were discovered in soft soil downhole sites during the 1995 Kobe earthquake (Japan), 1999 Chi-Chi earthquake (Taiwan), and 2000 Tottori earthquake (Japan). The analysis of downhole observations and stochastic finite-fault simulations indicated that the layers showed strong soil nonlinearity, resulting in a hysteretic stress-strain loop during the seismic wave propagation. Time-dependent shear modulus was also found in KiK-net Japan networks [45–49]. More recently, the physical nonlinearity of soils, manifested in a violation of the linear relationship of the dynamic shear stress-strain, can be roughly estimated by the ratio of the PGA versus the peak ground velocity (PGV) of the soil site station to the average shear wave velocity in the topmost 30-m surface soil layer (Vs30) (as an efficiency strain proxy [50]). The approach was verified in different seismological regions using various seismic indices, such as SA, shear modulus degradation, horizontal anisotropy of the shear wave, relative displacement-based strain, site-condition proxy for the basin depth, seismic velocity perturbation from the co-seismic velocity drop, index of the reduction of shear modulus, cumulative absolute velocity, and Arias intensity. The approach is useful in the analysis of soil nonlinearity, exclusion of possible records with the soil nonlinearity effect, and verification of the ability of nonlinear simulation tools [51–61]. Although a study indicated that the strain proxy might underestimate the maximum shear strain of soil, a clear sharp velocity impedance contrast exists [62].

The understanding on the characteristics of the two parameters, namely, the strain-dependent shear modulus $G$ and damping factor $h$ (inversely proportional to quality factor; $h = 1/2Q$), is important in soil nonlinearity studies. In this study, frequency-dependent damping ratios were calculated from the near-surface frequency-dependent $Q$ using the spectral ratios of a smoothed power spectrum using strong motion records in the station pairs of SMART1, in accordance with Peng and Wen [63]. Frequency-dependent quality factors have been widely identified by acceleration signals or coda waves since the 1980s in Taiwan [64–68] and by the general inversion technique (GIT) or spectral inversion method used in worldwide [69–74] for the discussions of site amplification factors or prediction of strong ground motions from stochastic simulations or random vibration theories in many regions [75–80]. In addition, despite the need for further links between the amplitude behavior of the frequency-dependent $Q$ and constant $Q$ [81], the importance of the frequency-independent constant $Q$, which was mentioned in studies finding the slope of spectral decays [82–84], still needs to be carefully discussed. However, the abovementioned frequency-dependent $Q$ studies mostly considered the comprehensive effect of the entire ray path through the seismic source to the site but not at the near-surface regions, and the resolution in the shallow region depends on the coverage of regional seismicity and stations. Furthermore, the strong motions of SMART1 were selected in this study because most of the variability of the site effect could be reduced as the distance

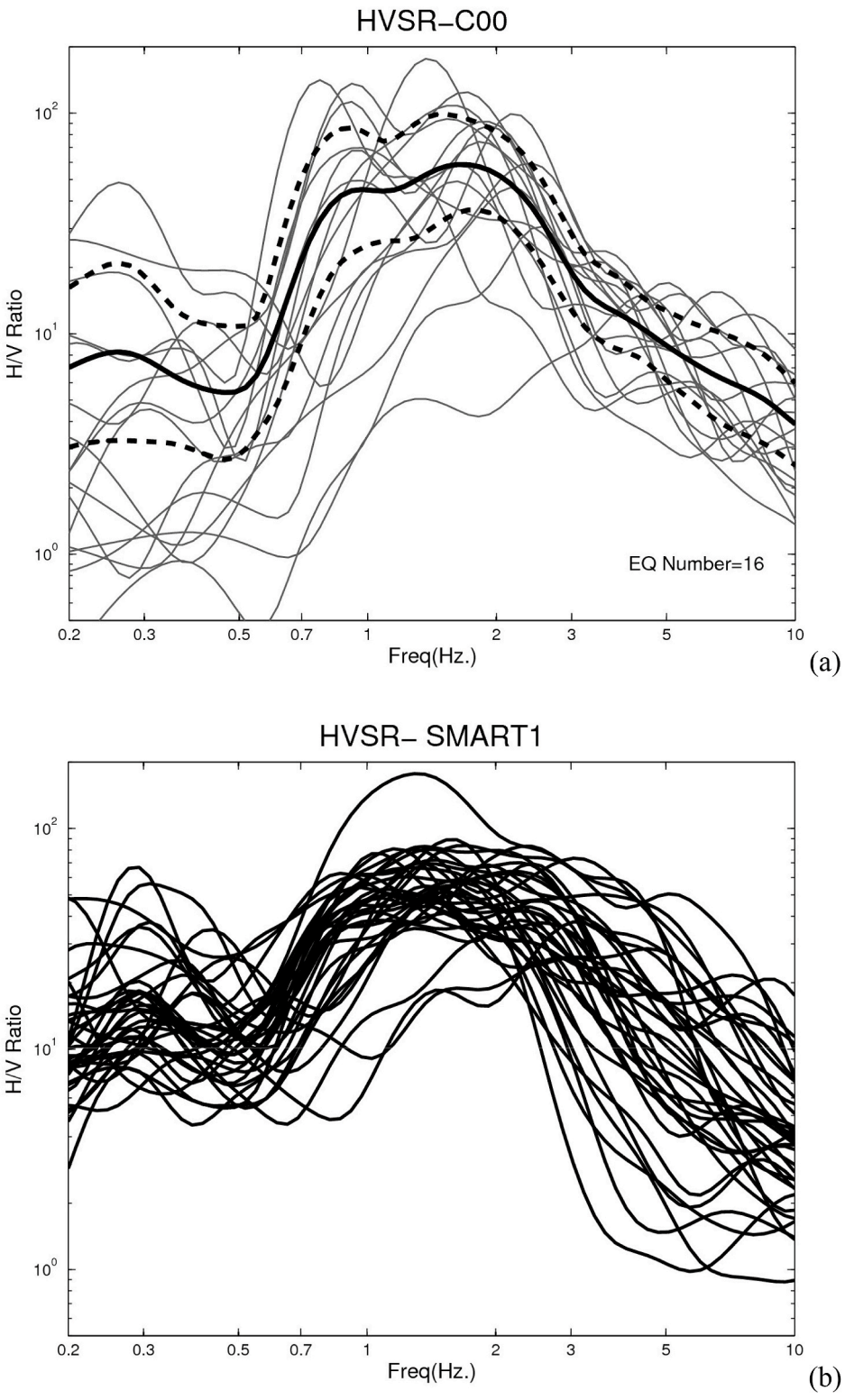


**Fig. 3.** HVSR of SMART1 used as a site amplification function in this study. (a) Sample HVSR of station C00. Gray lines are the HVSRs of the power spectrum for each weak motion; solid and dash black lines represent the mean and ± one standard deviation range. The mean HVSRs are calculated and used while the recording numbers were greater or equal to 10 to make sure that the site effect is representative for each station. (b) Mean HVSRs of each SMART1 station used in this study. Black lines indicate the mean HVSR of the weak motions of 35 SMART1 stations.

of the farthest station pairs was approximately 5 km (presented as triangles in Fig. 1), and many high-intensity records were recorded during the operating periods (1980–1990), which included 12 events with recorded PGAs greater than 100 gal in a total of 60 events with a high possibility of soil nonlinearity. In addition, while the proper damping factor, *h*, could be identified, Lee et al. showed that the soil nonlinearity effect could be reproduced from the equivalent linear method [85] in the LSST array if suitable *G* and *h* were obtained [86]. Wider applications and more accurate strong motion predictions could be generated using the frequency-dependent damping ratios built in this study, although the equivalent linear method might have shortcomings in predicting extremely high shear strains or the site has apparent liquefaction [87]. Beside, over-damped (underestimate) behaviors in high frequency band were reported in strong motion simulations [87,88] if we only consider frequency-independent *h* for equivalent linear method [85], and induced higher prediction uncertainty in high strain situations.

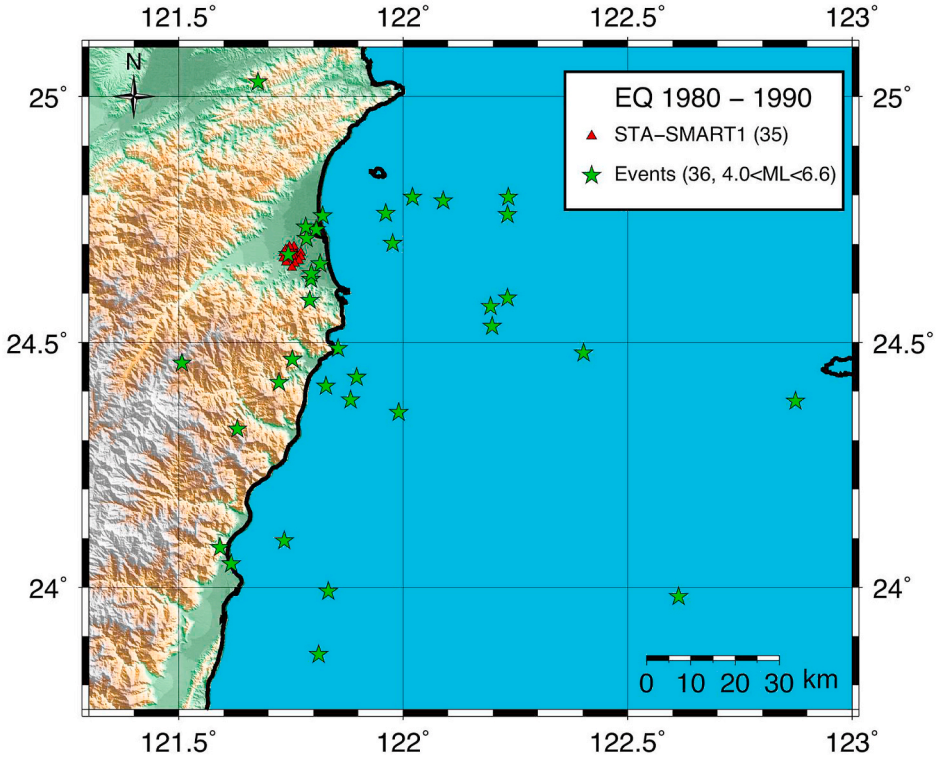


**Fig. 4.** Seismic events and stations used in this study in SMART1 with $M_L$ 4.0 to 6.6 from 1980 to 1990 in Taiwan. Numbers in parentheses denote the numbers of events and stations used.

Although it's very hard to discover the frequency-dependent h clearly from seismic observation since most of the energy might attenuate in many cases, some researches has reported and discussed the occurrence of the frequency-dependent *h* [12,89,90]. A frequency-dependent equivalent linear method [91,92] has once been introduced and updated [93] to solve the higher uncertainty in high frequency but still lack of observation supported. In this study, we than provide a possible way to prove occurrence of frequency-dependent h from seismic observation and might benefit the future ground motion simulations.

## 2. Methodologies and database

Peng and Wen mentioned that the near-surface frequency-dependent *Q* calculated from the SMART2 downhole data can be obtained by the spectral ratio of the smoothed power spectrum [63]. Theoretically, the frequency-dependent *Q* has a scaling of $f^n$ [94], and the calculation can be started from the power spectrum $S_i(f,R_i)$ of the S wave as [95]:

$$S_i(f,R_i) = S(f)Z(R_i)\exp\left[-\frac{2\pi f R_i}{vQ(f)}\right] \quad (1)$$

where *S(f)* is the source spectrum, *Z(R)* represents geometrical spreading at certain distances, *v* is the velocity of the shear wave, *Q(f)* is the frequency-dependent quality factor belonging to the propagation path, *R* is the distance from the source to the site, and *f* is the frequency. Furthermore, the orientation-independent horizontal power spectral is calculated as:

$$S_i(f) = \sqrt{\frac{1}{2}\left[PS_{EW,i}(f)^2 + PS_{NS,i}(f)^2\right]} \quad (2)$$

where $PS_{EW}$ is the power spectrum of the east-west component and $PS_{NS}$ is the north-south component. Smooth and downsampling processes from Konno-Ohmachi smoothing window [96], following the procedure proposed by Kottke et al. were applied to the $S_i(f)$ spectrum [97]. The calculation from each station pair between stations 1 and 2 can be listed as

$$\frac{S_1(f)}{S_2(f)} = \frac{Z(R_1)}{Z(R_2)}\exp\left[-2\pi f\frac{\Delta R}{vQ(f)}\right], \quad (3)$$

where $\Delta R$ is the distance difference between two ray paths from the source to the two stations that the *Q(f)* calculated here were corresponding to the final portion of the ray propagation of the farer station of each station pair in topmost layer with thickness equal to $\Delta R$, and *Q(f)* can be presented as

$$Q(f) = \frac{-2\pi f\Delta R}{v\cdot\ln\left(\frac{S_1(f)}{S_2(f)}\frac{Z(R_2)}{Z(R_1)}\right)} \quad (4)$$

in which *Q(f)* would theoretically be equal to $af^b$ with a linear relation of constants *a* and *b*. Finally, the frequency-dependent damping *h(f)* can be obtained from the following simple formula:

$$h(f) = 100\%\cdot 1/(2\cdot Q(f)) \quad (5)$$

Moreover, a pseudo-bending ray tracing method [98–100] was applied to calculate the traveling distances of ray paths from the source to the site in a one-dimensional (1D) velocity structure and three-dimensional grid for the $\Delta R$ calculation. The 1D velocity structure (Fig. 2 and Table 1) was obtained from Taiwan's Central Weather Bureau for deep parts (2 km–280 km [101]), and shallow velocities were inverted from a diffuse elastic wave-field method [102,103] using microtremor HVSR (MHVSR) measurements (below 0.8 km [104]). The dense microtremor measurements conducted in Taiwan were completed in the 2000s and covered most of the alluvium regions [105], which were applied in many useful engineering seismology studies [58, 106–111]. The distribution of the microtremor measurements near SMART1 is marked as diamond symbols in Fig. 1, and the mean velocity structures inverted from 31 MHVSRs located within a 3 km radius from the center of SMART1 (dark-gray diamonds in Fig. 1) were used for the shallow part of the 1D velocity structure (Fig. 2) in this study.

**Table 2**
Events recorded in SMART1 and used in this study.

| Eq. no. | Year | Month | Day | Hour | Minute | Second | Lon | Lat | Dep | $M_L$ |
|---|---|---|---|---|---|---|---|---|---|---|
| 2 | 1980 | 11 | 14 | 13 | 37 | 4 | 121.7915 | 24.5857 | 62.1 | 5.5 |
| 5 | 1981 | 1 | 29 | 4 | 51 | 36 | 121.8963 | 24.4292 | 11.1 | 5.9 |
| 8 | 1981 | 3 | 10 | 8 | 24 | 51 | 121.7827 | 24.7345 | 7.1 | 4 |
| 10 | 1981 | 5 | 3 | 19 | 19 | 51 | 121.9762 | 24.702 | 68.5 | 4.4 |
| 12 | 1981 | 8 | 20 | 19 | 3 | 28 | 121.7438 | 24.6783 | 0.1 | 4.3 |
| 14 | 1981 | 8 | 30 | 18 | 54 | 53 | 121.7528 | 24.4653 | 0.2 | 4.3 |
| 17 | 1982 | 2 | 21 | 6 | 4 | 37 | 121.8208 | 24.7578 | 0.8 | 4 |
| 18 | 1982 | 2 | 28 | 13 | 23 | 32 | 121.806 | 24.7298 | 10 | 4.4 |
| 19 | 1982 | 4 | 1 | 4 | 50 | 2 | 121.8553 | 24.4872 | 7.9 | 4.3 |
| 20 | 1982 | 12 | 17 | 2 | 43 | 1 | 122.874 | 24.3807 | 29.2 | 6 |
| 22 | 1983 | 5 | 10 | 0 | 15 | 3 | 121.5073 | 24.4582 | 1.2 | 6 |
| 24 | 1983 | 6 | 24 | 9 | 6 | 42 | 122.6133 | 23.9815 | 25 | 6.6 |
| 28 | 1984 | 4 | 18 | 1 | 34 | 18 | 122.2338 | 24.7957 | 5.9 | 5.4 |
| 29 | 1984 | 4 | 23 | 22 | 35 | 4 | 122.089 | 24.7885 | 8.7 | 5.6 |
| 30 | 1984 | 12 | 29 | 1 | 7 | 2 | 122.0212 | 24.7958 | 60.7 | 5.9 |
| 31 | 1985 | 3 | 9 | 19 | 51 | 0 | 122.2325 | 24.7598 | 4.1 | 5.5 |
| 32 | 1985 | 6 | 12 | 13 | 23 | 13 | 122.2322 | 24.5902 | 5.3 | 5.5 |
| 33 | 1985 | 6 | 12 | 17 | 22 | 50 | 122.1947 | 24.573 | 3.3 | 6.1 |
| 34 | 1985 | 8 | 5 | 13 | 0 | 38 | 121.8828 | 24.3825 | 1.3 | 5.4 |
| 35 | 1985 | 8 | 12 | 0 | 21 | 33 | 121.785 | 24.7118 | 8 | 5.2 |
| 36 | 1985 | 9 | 20 | 15 | 1 | 24 | 122.1978 | 24.5328 | 6.1 | 5.9 |
| 37 | 1985 | 10 | 26 | 3 | 30 | 39 | 121.8283 | 24.4112 | 1.7 | 4.7 |
| 39 | 1986 | 1 | 16 | 13 | 4 | 31 | 121.9612 | 24.7628 | 10.2 | 6.1 |
| 40 | 1986 | 5 | 20 | 5 | 25 | 49 | 121.5915 | 24.0817 | 15.8 | 6.2 |
| 41 | 1986 | 5 | 20 | 5 | 37 | 31 | 121.6173 | 24.0482 | 21.8 | 5.8 |
| 42 | 1986 | 7 | 17 | 0 | 3 | 33 | 121.815 | 24.6598 | 2 | 4.3 |
| 43 | 1986 | 7 | 30 | 11 | 31 | 47 | 121.7942 | 24.6288 | 1.5 | 5.8 |
| 44 | 1986 | 7 | 30 | 11 | 38 | 31 | 121.7955 | 24.6397 | 2.3 | 4.3 |
| 45 | 1986 | 11 | 14 | 21 | 20 | 4 | 121.8332 | 23.9918 | 15 | 6.5 |
| 48 | 1986 | 11 | 15 | 0 | 17 | 42 | 121.8113 | 23.8627 | 7.6 | 4 |
| 49 | 1986 | 12 | 10 | 23 | 55 | 22 | 121.6763 | 25.03 | 98.6 | 5.2 |
| 53 | 1987 | 6 | 27 | 7 | 38 | 55 | 121.631 | 24.3235 | 0.5 | 5.1 |
| 54 | 1987 | 11 | 10 | 4 | 33 | 9 | 121.7237 | 24.418 | 34.4 | 4.9 |
| 55 | 1988 | 9 | 18 | 15 | 38 | 25 | 122.4015 | 24.4785 | 62.5 | 5.4 |
| 57 | 1990 | 4 | 15 | 22 | 44 | 9 | 121.99 | 24.3568 | 22 | 4.6 |
| 58 | 1990 | 11 | 11 | 23 | 59 | 6 | 121.7355 | 24.0952 | 34.3 | 5.4 |

*Information was collected from SMART1 websites maintained by the IES, Academia Sinica, Taiwan. (http://www.earth.sinica.edu.tw/content/labs/slab/smdmc/smart1/smart1.htm).

**Table 3**
Strong motion stations of SMART1 and used in this study.

| Station name | Longitude | Latitude | Station name | Longitude | Latitude |
|---|---|---|---|---|---|
| C00 | 121.7524 | 24.6776 | M06 | 121.7555 | 24.669 |
| E01 | 121.7522 | 24.6526 | M07 | 121.7498 | 24.6687 |
| I01 | 121.7528 | 24.6793 | M08 | 121.7461 | 24.6709 |
| I02 | 121.7538 | 24.6789 | M09 | 121.743 | 24.6742 |
| I03 | 121.7544 | 24.6782 | M10 | 121.7435 | 24.6789 |
| I04 | 121.7545 | 24.6772 | M11 | 121.7452 | 24.6837 |
| I05 | 121.754 | 24.6764 | M12 | 121.7496 | 24.6863 |
| I06 | 121.7529 | 24.6759 | O01 | 121.7565 | 24.6955 |
| I07 | 121.752 | 24.6759 | O03 | 121.7718 | 24.683 |
| I08 | 121.7513 | 24.6763 | O04 | 121.7717 | 24.6742 |
| I09 | 121.7506 | 24.677 | O05 | 121.7676 | 24.666 |
| I11 | 121.7512 | 24.6787 | O06 | 121.7586 | 24.6603 |
| I12 | 121.7519 | 24.6793 | O08 | 121.7396 | 24.6633 |
| M01 | 121.7545 | 24.6864 | O09 | 121.7335 | 24.6714 |
| M02 | 121.7594 | 24.6852 | O10 | 121.7332 | 24.6817 |
| M03 | 121.7612 | 24.6807 | O11 | 121.7383 | 24.6895 |
| M04 | 121.7623 | 24.6756 | O12 | 121.7467 | 24.6948 |
| M05 | 121.7598 | 24.6721 | | | |

*Information was collected from SMART1 websites maintained by the IES, Academia Sinica, Taiwan. (http://www.earth.sinica.edu.tw/content/labs/slab/smdmc/smart1/smart1.htm).

In addition, acceleration records with PGAs within 2.5 gal to 60 gal were chosen to prevent soil nonlinearity in the mean S-wave HVSR calculation from weak motions at each site in SMART1 (Fig. 3 (a)), which were treated as site amplification functions and were eliminated site by site from $S_i(f)$ in Eq. (3). The HVSR of each station in SMART1 showed a dominant frequency range from 0.7 Hz to 2 Hz (Fig. 3 (b)). Similar HVSR shapes and amplification levels were found, but they did not indicate large variance in the linear site response.

Furthermore, SMART1 consisted of three concentric circles with a spacing radius of 200 m, 1 km, and 2 km and two short arms, with a total of 41 stations (Fig. 1), and 60 events were recorded during the operation period from 1980 to 1990. Each of the two stations was composed of a station pair used to calculate the spectral ratios of the smoothed power spectrum. Seismic events were used, and the difference between the horizontal incident angle and angle of each pair was less than 20°. Meanwhile, five stations in SMART1 were eliminate as the record numbers corresponding to the abovementioned criteria were less than 10; a total of 35 stations, 36 events, and 608 records were used in this study (Fig. 4; Tables 2 and 3). Examples of data processing for frequency-dependent $Q$, calculated from Eq. (4) of station pairs C00 and O01, are plotted in Fig. 5. Three events were recorded from the station pair in the database within abovementioned 20° incident angle ranges. One of the events (Earthquake number 40, EQ40) might have a larger chance to respond to the soil nonlinearity owing to the large intensity recorded in the sample station pairs (PGA over 200 gal) and reflected lower $Q(f)$ on the shallow layers as compared to the other two records with weaker motions. The $Q(f)$ calculated here represents the response of the top shallow layers and its thickness were equal to $\Delta R$, which were identified by subtracting the travel distances of the two ray paths of the same events. Although the spectral ratio method might eliminate the source effect in general, some source variabilities might influence the frequency band below the corner frequency. The frequency band lower than the corner frequency of each event was not considered in obtaining $Q(f)$. The corner frequency $f_c$ of the theoretical source spectrum followed

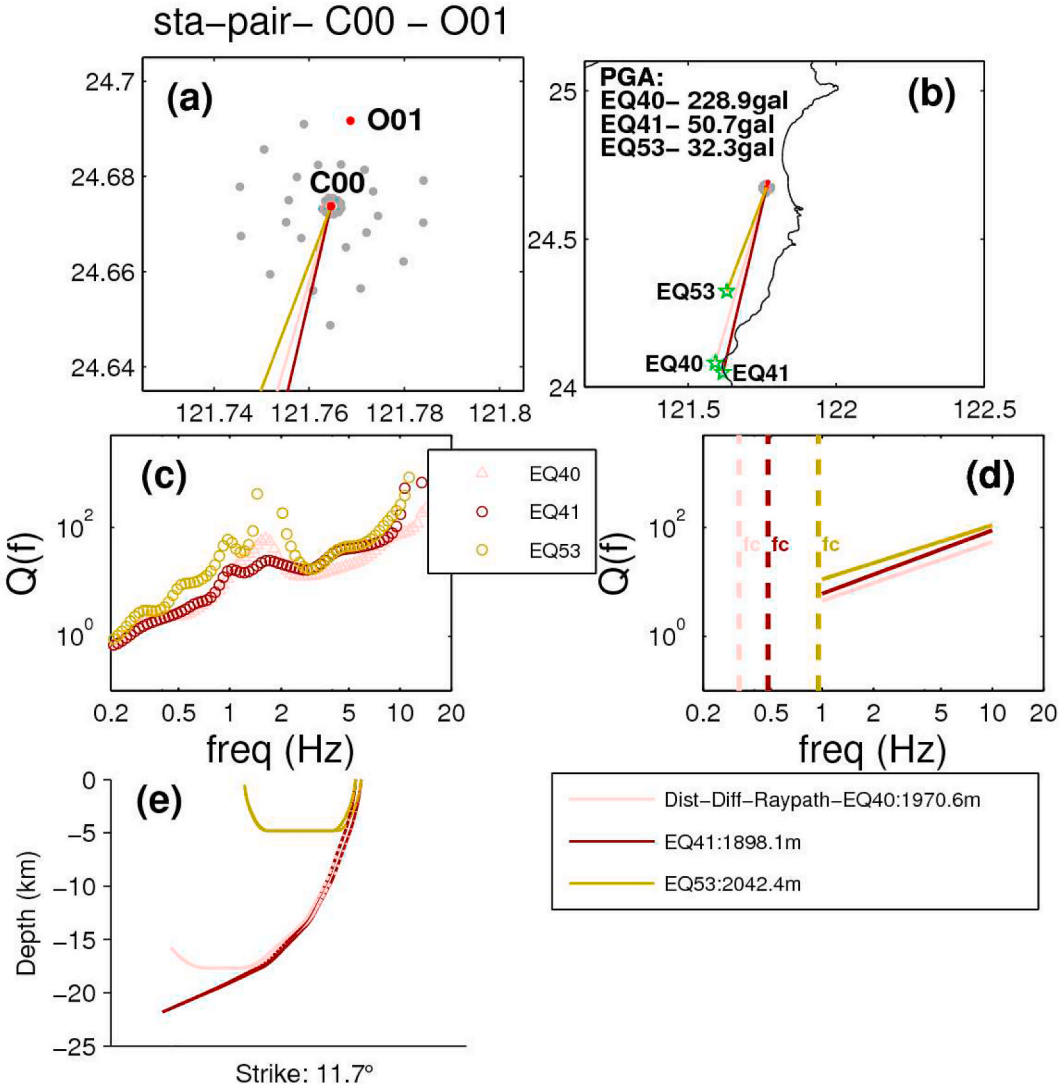


**Fig. 5.** Sample procedures of the *Q(f)* calculation of station pairs C00 and O01 in SMART1. (a) Locations of SMART1 stations and ray paths of the recorded events. Red dots are station pairs C00 and O01, gray dots are other SMART1 stations, and coloring lines indicated the ray path of three events. (b) Locations of events and ray paths recorded in the station pairs. Green stars are the epicenters; the PGAs of these events recorded in the pairs are marked in the upper-left portion. (c) Frequency-dependent *Q* calculated from the spectral ratio of the power spectra for the three events. Colors correspond to the abovementioned events and ray paths. Triangles represent the recorded PGAs greater than 100 gal, and circles represent those less than 60 gal. (d) Solid lines represented the *Q(f)* of the three events. Colors represent the same entities as previous figures. Dashed lines indicated the corner frequency calculated from the theoretical source spectrum. (e) Projections of the underground ray path of the three events on a 11.7° strike plane. Legends indicated the event numbers and the difference of travel distances between each source toward two station pairs. (For interpretation of the references to color in this figure legend, the reader is referred to the Web version of this article.)

Aki [112] and Brune [113], as described in Boore [12], and can be listed as

$$f_c = 4.9 \times 10^6 \beta \left( \Delta\sigma / M_0 \right)^{1/3} \tag{6}$$

where $\beta$ is the shear wave velocity (3.6 km/s [80]), $\Delta\sigma$ is the stress drop (80 bar [80]), and $M_0$ is the seismic moment (dyne-cm) calculated from $M_L$ ($log_{10}(M_0) = 1.27M_L + 17.23$ [114]). Therefore, the frequency band between 2 or $f_c$ (the larger one as the minimum of the band) and 10 Hz was used for frequency-dependent *Q(f)* calculation to prevent possible variabilities from the site effect and source effect (Fig. 5(d)). *Q(f)* of SMART1 used in this study is shown in Fig. 6. A reasonable *Q* range of the mean $Q(f) = 15.1f^{0.9}$ was found, although variances of *Q* in the individual records were still large. Finally, because Vs30 could be inverted from the abovementioned MHVSR in the SMART1 region, the strain proxy (PGV/Vs30) was calculated to check the nonlinearity of the frequency-dependent damping h(f). A nonlinear shear stress-strain relation was clearly found in SMART1 based on the PGA and PGV/Vs30 relation in a range from PGA of 17.4–375.2 gal and PGV of 0.59–43.98 cm/s (Fig. 7 (a)). Furthermore, DNL [34,35] was calculated and shown in Fig. 7 (b) to double-check the frequency behavior of soil nonlinearity of the SMART1 records used in this study as followed:

$$\mathrm{DNL} = \sum \left| \log \left( \frac{R_{strong}}{R_{ref}} \right) \right| \Delta f \tag{7}$$

where $R_{strong}$ means S-wave HVSR for each strong motion and $R_{ref}$ is S-wave HVSR for the mean of reference weak motions for the same site. $\Delta f$ means frequency interval and the DNL is summed from 0.5 to 20 Hz. In general, it indicated that soil nonlinearity becomes apparent when the following situation occurred such as strain proxy is greater than 0.03%, PGA is greater than 100 gal or DNL is greater than 5 to 6 in this region (Fig. 7).

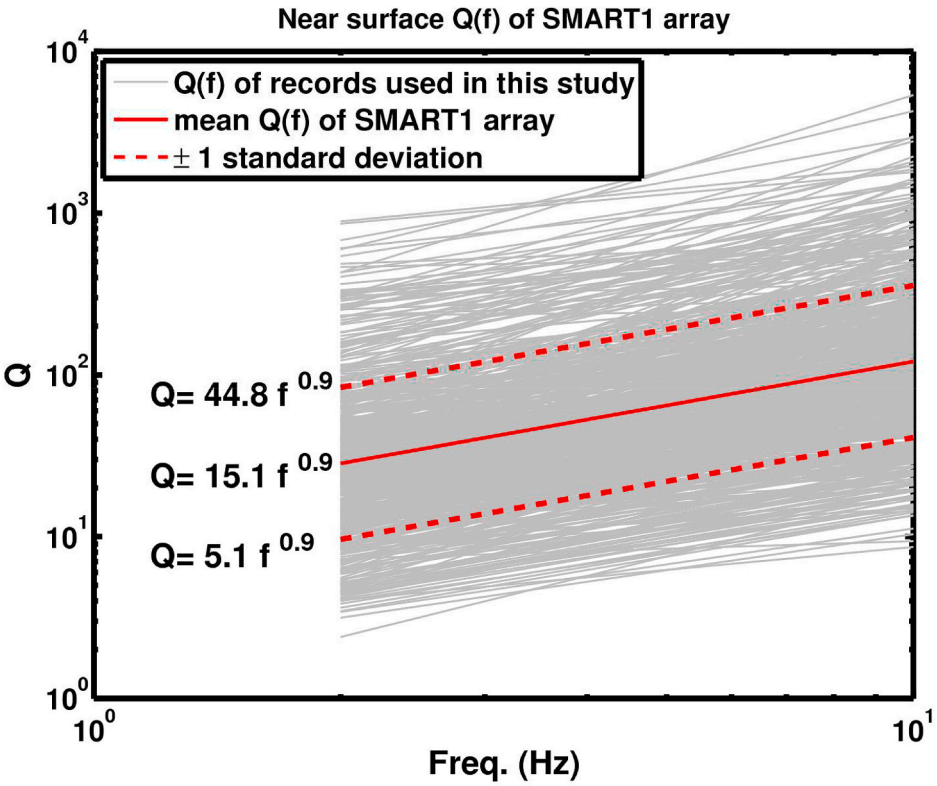


**Fig. 6.** Frequency-dependent quality factor calculated from the spectral ratio of the power spectrum for SMART1. Gray lines are the *Q(f)* of each record from individual station pairs, red lines are the average and ± one standard deviation *Q(f)* for near-surface structures in SMART1. (For interpretation of the references to color in this figure legend, the reader is referred to the Web version of this article.)

## 3. Results and discussions

Fig. 5 (c) indicates that *Q(f)* from the spectral ratio of the two surface stations of SMART1 was not a totally straight line as $af^b$ functions, especially in the lower-frequency band, which might be disturbed by the source effect and site effects. Abrahamson used the frequency-wavenumber (F–K) method to identify wave scattering as a means of wave propagation through SMART1 that induced uncertainty in the incident angles of each event [115]. An incoherent wave propagation in the S-wave portion for a sample event was found owing to the possible wave scattering within the array or multiple refractions passing through the complex velocity structures that led to a 30° difference in incident angles during the first 3 s of the S arrival. More uncertainties might be induced within the SMART1 region, which would influence the spectral ratio calculations of each station pair in this study, resulting in some incoherent shapes in the frequency-dependent *Q*. Therefore, the regression of *Q(f)* from the frequency band approximately 2 Hz or greater than $f_c$ to 10 Hz was used in this study to evaluate the soil nonlinearity response in the damping for near-surface sedimentary layers. A lower *Q(f)* was found from the larger-intensity records for a similar $\Delta R$ of the sample station pairs shown in Fig. 5(d), which represents a higher damping (lower *Q*) occurring during stronger shakes for similar ray paths through near-surface shallow structures. $\Delta R$ is the distance difference in Fig. 5(e), where the distance subtraction between longer and shorter paths reflected the topmost layers underneath the two sites. *Q(f)* calculated in this study indicated a mean ± one standard deviation range of *Q* equal to 5 to 45 times $f^{0.9}$ in the SMART1 region (Fig. 6). This result showed a similar range of frequency-independent *Q*, such as $Q = 55.11 \pm 15.1$ in the SMART1 region [116], *Q* below 150 from the *Q* tomography result below a 1 km depth in this region [82], and a lower frequency-dependent *Q* accompanied with the same power as compared to the average *Q(f)* of larger regions (e.g., $Q = 80f^{0.9}$) for shallow structures in Taiwan used in Huang et al. [80] as a near-surface shallower structure should have a weaker quality than deeper structures. However, the exact corresponding frequency band between the frequency-dependent and independent *Q* could not be directly compare with the *Q* value.

Furthermore, the strain-dependent damping *h(f)* was separately checked in different frequencies, such as 2, 3, 5, and 8 Hz. The combination of $\Delta R$ from short-, middle-, and far-distance records was divided from distance of 500 m and 2 km to check that the layers generated significant nonlinearity in the *h(f)* calculation (Fig. 8). Owing to the limitation of station interval of SMART1 and operation time period that there's no enough records could be displayed in short distance group, we aimed to explain the statistically confidence of the mean damping curve, the 95% confidence intervals [117] of the mean damping curve from regression procedure were shown in dash lines in Fig. 8 and were calculated as followed:

$$\hat{y}_{ci} = \hat{y}_{ai} \pm S_e \sqrt{2F\left[\frac{1}{n} + \frac{\left(x_i - \overline{X}\right)^2}{\sum_{i=1}^{n}\left(x_i - \overline{X}\right)^2}\right]} \tag{8}$$

where $\hat{y}_{ci}$ means the confidence level of the damping *h*, $\hat{y}_{ai}$ is the estimated regression lines of the *h*, $S_e$ is standard error of estimate, F means critical values for the F distribution (Joint hypothesis test, f-test), n is the sample numbers, $x_i$ means individual effective strain value (PGV/Vs30) in x axis, $\overline{X}$ is mean of the effective strain value, both axes were calculated in log 10 unit. The results indicated we have larger variance in higher strain owing to the lack of the high intensity earthquakes during the operated time period of SMART1, and larger variance in shorter $\Delta R$ which is relate to distance of those station pairs was not close enough to capture much short $\Delta R$ records. However, the overall trends indicate a positive trend in damping-strain relations of shorter $\Delta R$. In general, owing to the complexity of the mean response of the whole shallow

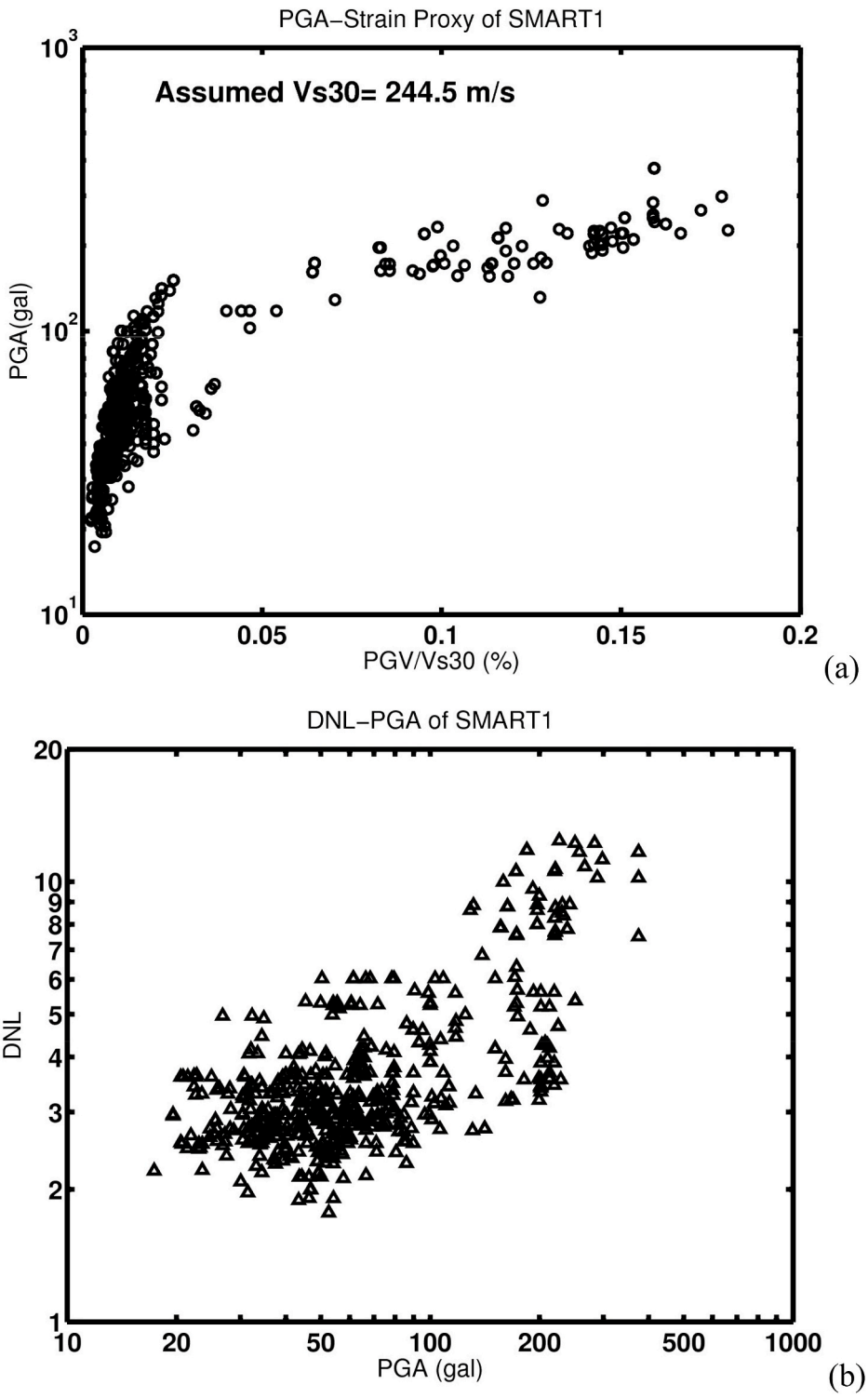


**Fig. 7.** (a) Stress-strain relation calculated from the PGA and PGV/Vs30 as a strain proxy of the SMART1 records used in this study. Vs30 is 244.5 m/s (Fig. 2). (b) Soil nonlinearity checked from DNL-PGA relation of the SMART1 records.

layers reflected in the spectral ratios between each two surface stations, the sharp change in damping was not identified in this study, but a clear proportional trend could be found in the shorter $\Delta R$, which means that the shallow layers of the topmost 500 m layers hold the main soil nonlinearity effect from the damping increase while the strain increases. Clearly, the topmost 500-m layers in the SMART1 region belonging to the softer soil layers (Vs less than 1 km/s in Fig. 2) might respond significantly to soil nonlinearity compared with the higher Vs layers. Furthermore, several features could be identified in Figs. 8 and 9. For instance, a lower frequency reflected a larger damping, and increasing damping relations were found in larger strains in the main shorter $\Delta R$, but these might be dissipated or get an opposite response owing to the mean response of the deeper structures in the middle and far $\Delta R$ records. Smaller variances in the larger strain records in all frequency bands indicated that soil nonlinearity mainly controls the damping response in the high strain. In contrary, higher variability of the damping scaling in

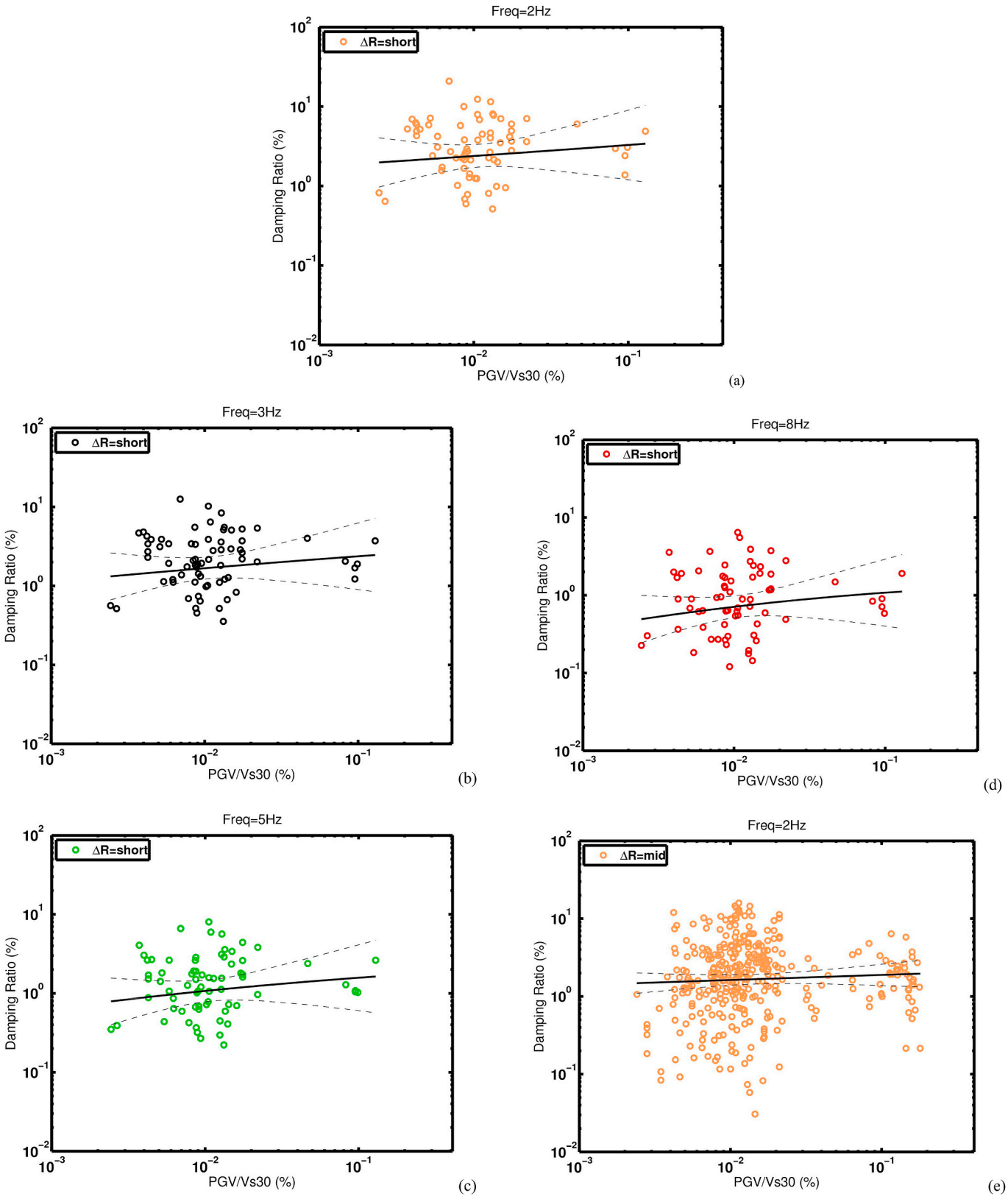


**Fig. 8.** Relation of the damping ratio h(f) and strain proxy PGV/Vs30 at certain frequencies in different distance differences between two ray paths (ΔR). Dashed lines are 95% confidence interval of the regression line. ΔR less than 500 m are the short distances, ΔR 500 m to 2 km are the middle distances and ΔR greater than 2 km are the far distances. (a) 2 Hz at a short distance, (b) 3 Hz at a short distance, (c) 5 Hz at a short distance, (d) 8 Hz at a short distance, (e) 2 Hz at a middle distance, (f) 3 Hz at a middle distance, (g) 5 Hz at a middle distance, (h) 8 Hz at a middle distance, (i) 2 Hz at a far distance, (j) 3 Hz at a far distance, (k) 5 Hz at a far distance, (l) 8 Hz at a far distance.

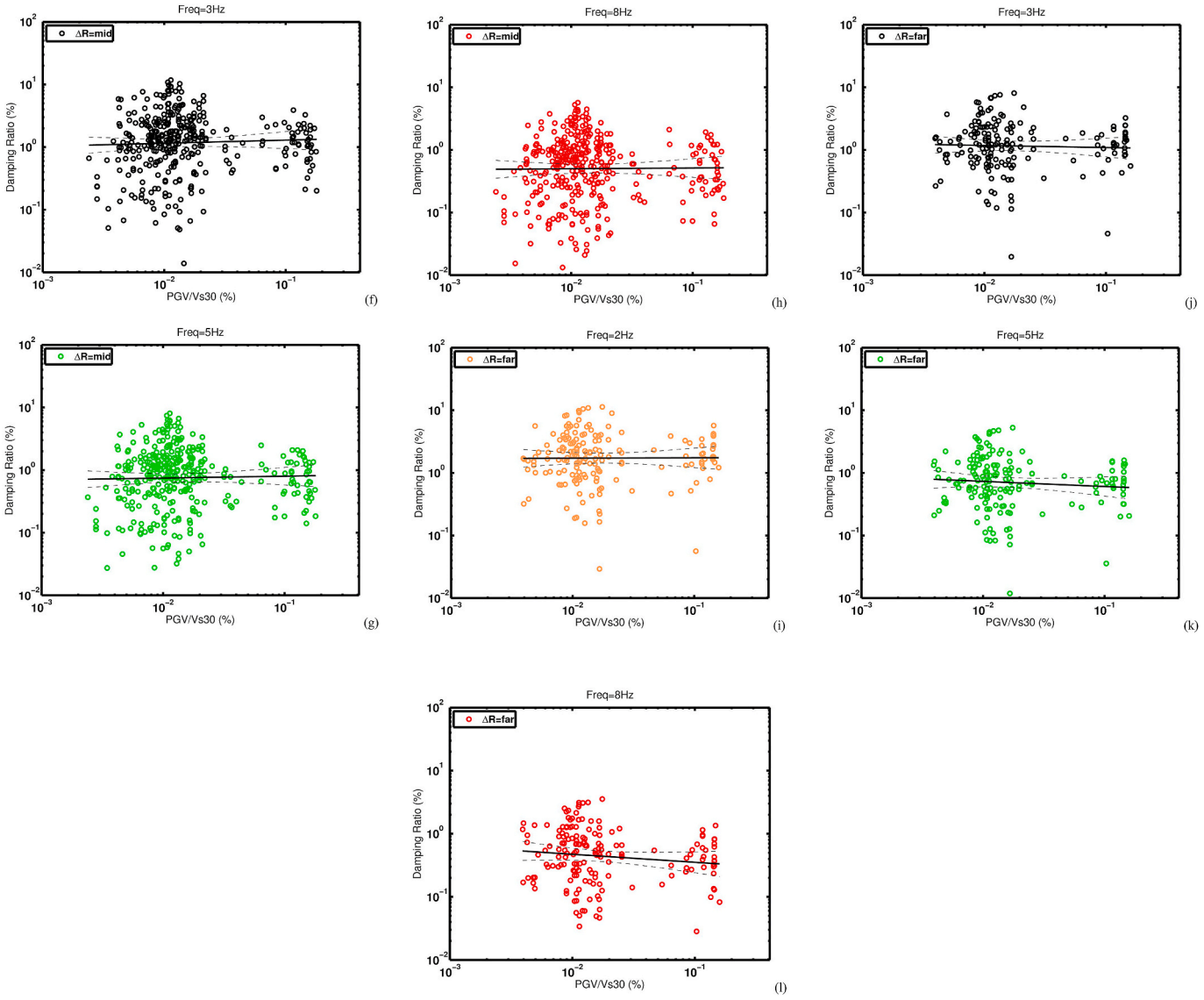


**Fig. 8.** (*continued*).

the smaller strain records might relate to the following uncertainties such as 1. Geometry distribution and interval distances of SMART1 stations was a range from 200 m to 4 km and Δ*R* of two ray paths belong to the station pairs has larger range of 300 m to 6 km. That means while the decomposed Q/damping from spectral ratio method were extracted from topmost layers that larger ΔR might induce larger variations. 2. The incident angles of seismic sources recorded in SMART1 were covered in wide range of directions (Fig. 4) toward a 2D circular array that means Q/damping of the considered ray paths represented average of 3D site response in this region and were corresponding to combination effects of 3D subsurface layers. Meanwhile, as described in previous sections, previous study [115] indicated wave scattering in SMART1 region that might relate to 3D site response and induced some variability. 3. Owing to the near surface Q/damping calculated in this study were topmost layers of a range from 300 m to 6 km that means the represented phenomenon was mixed effect from different proportion of soil and rock of each layers. However, we thought the variability of Vs and Q/damping in near surface layers should be included while considering 3D site response or using 1D site response to capture real response in 3D subsurface structures. In this study, owing to it's very hard to get the core samples for experiments greater than 300 m to 3 km or more from deep borehole to directly examine the observed trend, that we try to provide a reasonable estimation method to capture possible variability of topmost layers. In addition, owing to some limitations due to the short operation time period, insufficient large strain data could be observed in SMART1 as compared with the higher strain response in the laboratory experiments. The apparent 40%–50% increase in damping *h (f)* at each frequency was identified with strain proxy from 0.01% to 0.1% in Fig. 9 for short Δ*R* (solid lines). Moreover, the damping curve of short Δ*R* showed a smaller response compared to that used in the equivalent linear method for soils shallower than 47 m in LSST [86] because Δ*R* resolved in the SMART1 region indicated a range of 100 m–500 m in this study, which was slightly deeper than the scale of traditional geotechnical coring experiments. For instance, a depth-dependent damping curve models were established for soil behavior with a general depth range of up to 300 m in Eastern North America (denoted as EPRI93 [118]). The damping curves for short Δ*R* developed in this study showed similar responses at 3–5 Hz below a strain of 0.03% indicating that the mean response discovered below 500 m might extend a steeper trend in the larger strain as the trend in the EPRI93 model if larger seismic observations exist (Fig. 9). Furthermore, basic site effect opinions indicated thicker layers would response in lower frequency ground motions that means high frequency results might not dominant by deeper structures such as far ΔR group. High

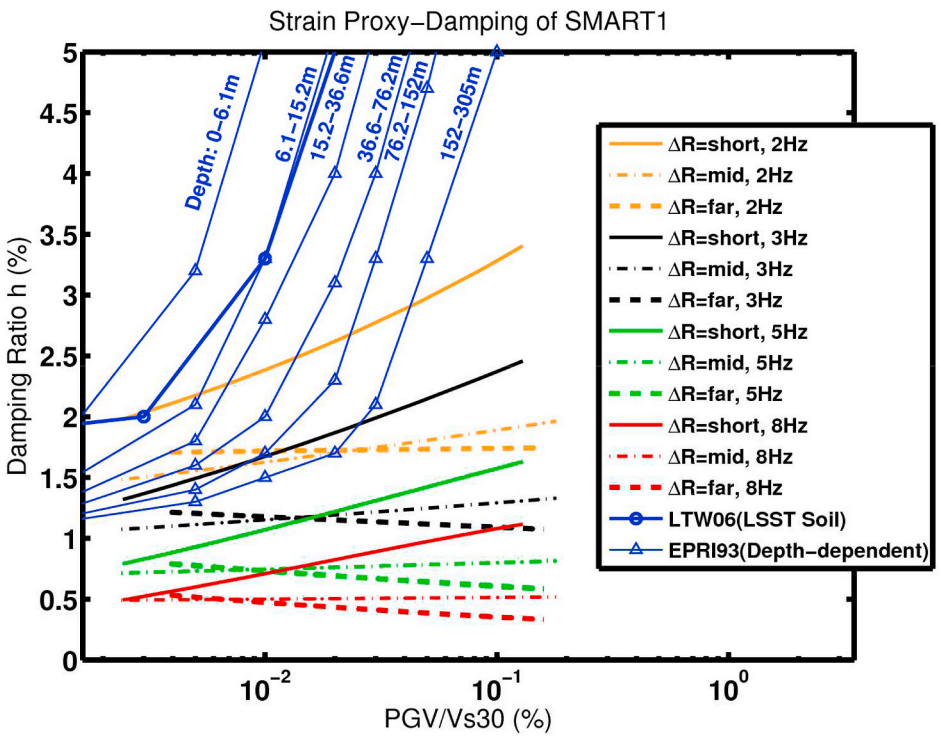


**Fig. 9.** Trend relation of the damping ratio *h(f)* and strain proxy PGV/Vs30 at certain frequencies in different distance differences between two ray paths ($\Delta R$). Same definitions of $\Delta R$ were used in Fig. 8. LTW06 is the damping curve used for the equivalent linear method for the soil condition in the LSST downhole array [86]. EPRI93 is a group of depth-dependent damping curve for shallow subsurface layers for gravelly sand or sandy clay. The corresponding depth levels are marked in blue words [118]. (For interpretation of the references to color in this figure legend, the reader is referred to the Web version of this article.)

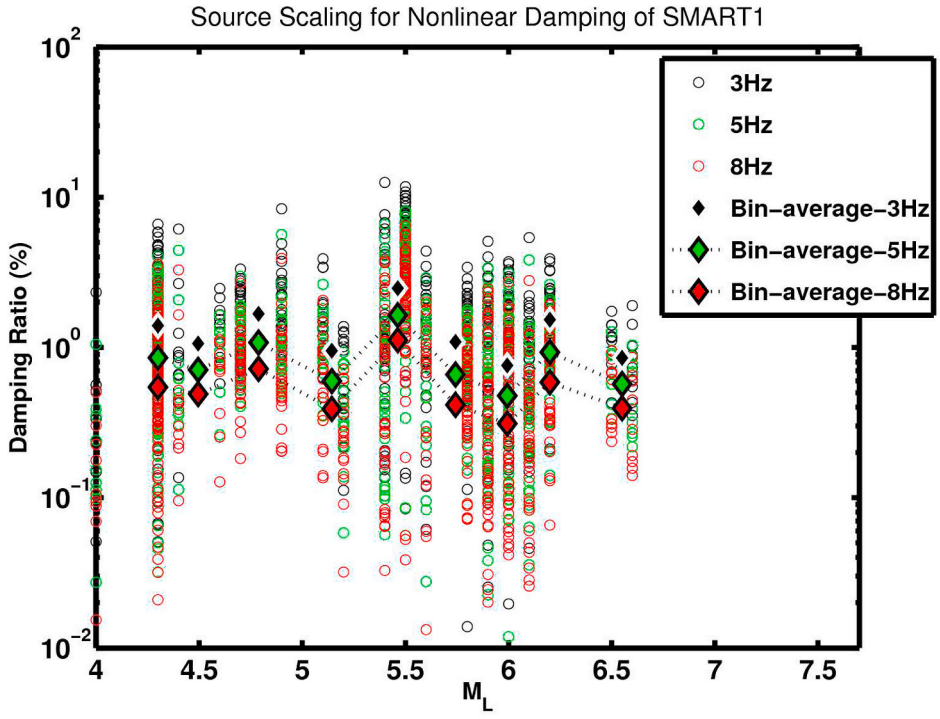


**Fig. 10.** Magnitude scaling relation of the frequency-dependent damping showed in SMART1. Circles are the damping calculated from the records; triangles are the binned average of each $M_L$ bins. The colors represent different frequencies. (For interpretation of the references to color in this figure legend, the reader is referred to the Web version of this article.)

frequency ground motions may be biased from other effects and generated larger variability in Fig. 8i, j, k, l. Meanwhile, deeper structures may not suffer from large strain while ground motion intensity would be much smaller in very hard rock at deep structures. Therefore, the trend of damping curves for middle and far from 2 to 8 Hz were basically flat and might be biased from other effect such as path attenuation or wave scattering in the SMART1.

In addition, the scaling relations of the source, path, and site effects were examined for the damping *h(f)* in Figs. 10–13 to ensure the main influences. There is no clear connection between the magnitude scaling and damping ratio. As expected, the damping ratio should have more correlation with the site effect. Binned averaged damping showed two

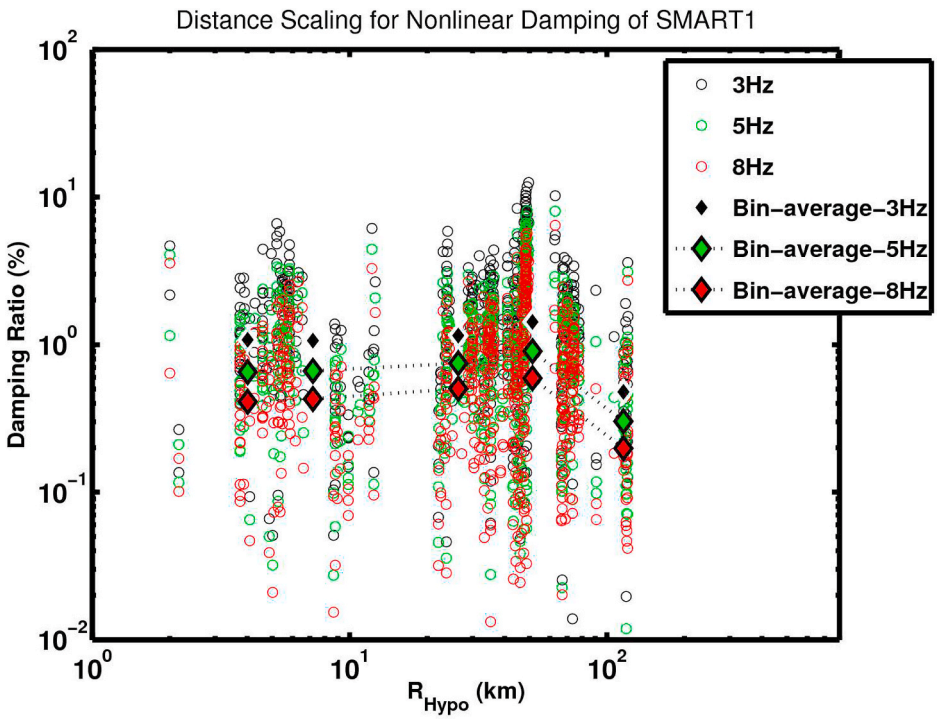


**Fig. 11.** Distance scaling of the frequency-dependent damping showed in SMART1. Symbol descriptions are described in Fig. 10.

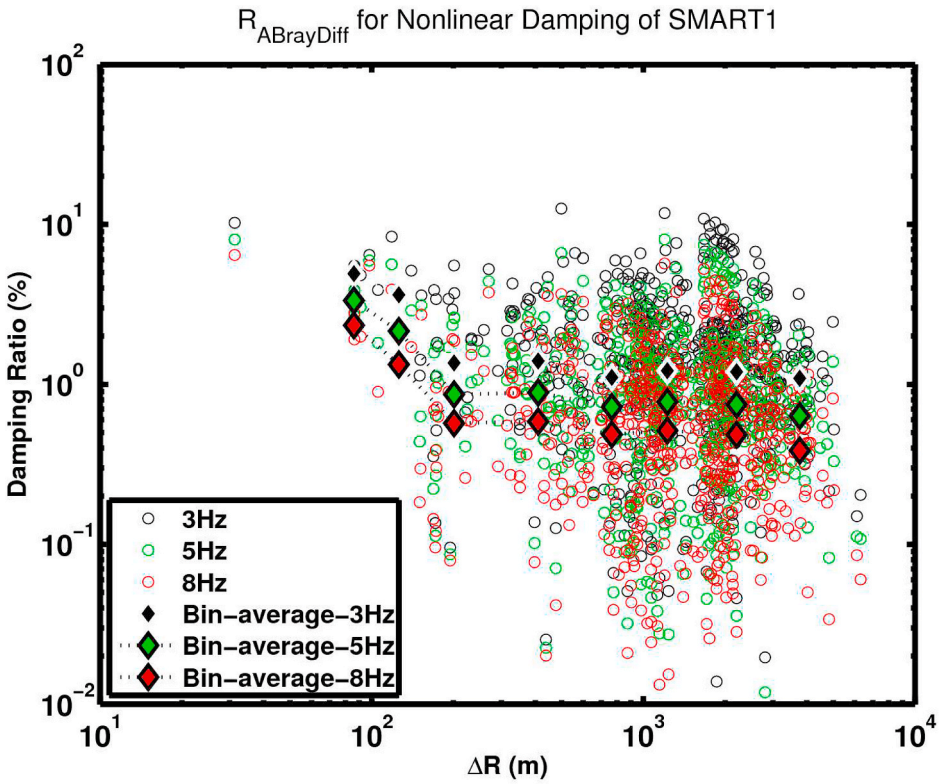


**Fig. 12.** Scaling of the difference of traveling distances ($R_{ABrayDiff}$, $\Delta R$) between two ray paths for each station pair of frequency-dependent damping showed in SMART1. Symbol descriptions are described in Fig. 10.

features: larger damping occurred in lower-frequency results and large variances with different $M_L$ and was generally independent of it from $M_L$ 4 to 6.6 (Fig. 10). Moreover, small correlations might occur in the path effect found from the distance scaling, binned averaged damping indicated a similar level below 70 km from the hypocenter distance ($R_{Hypo}$), and a significant drop in longer $R_{Hypo}$ results might possibly be related to the surface wave generation. Moreover, the hypocentral distances were greater, and this array was located on the soft sedimentary

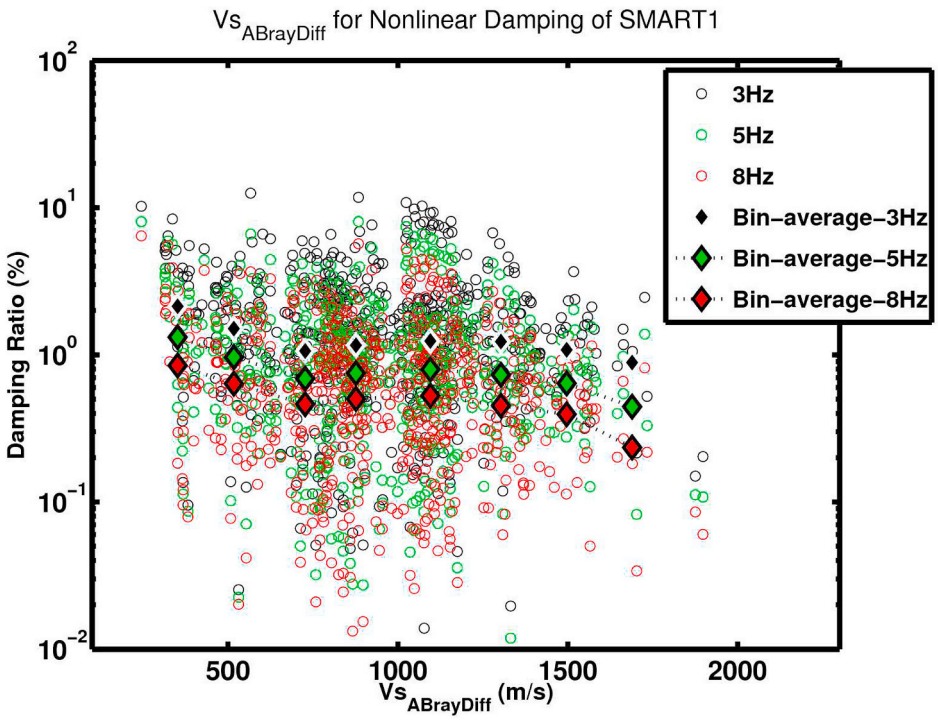


**Fig. 13.** Scaling of the mean Vs of the velocity structures for layers upon Δ*R* depth compared with the frequency-dependent damping showed in SMART1. Symbol descriptions are described in Fig. 10.

Ilan Plain and thus might enlarge the seismic energy accompanied by smaller damping ratios for near-surface layers (Fig. 11). Finally, the site effect related to the scaling from the traveling depth and shear wave velocity of the near-surface layers indicated a clear dependency for the damping ratio *h(f)*. Although not much data were observed in Δ*R* smaller than 100 m owing to the limitation of operating period and minimum radius of the free-field stations in SMART1, damping increases in all frequencies resulted in a binned average below 200 m, as shown in the scaling of the difference of traveling distances, and another drop occurred at approximately 500 m depth (Fig. 12) that corresponded to the abovementioned apparent damping increase in the short Δ*R* group in Fig. 8. For a larger difference in ray paths, a smaller damping occurred, which means that the spectral ratio consisted more of high-*Q* materials in deeper layers, where the average response would be influenced. By contrast, the corresponding Vs for the higher damping records were generally at subsurface layers below a mean Vs of 600 m/s and might be biased from the path effect in the group with a mean Vs greater than 1400 m/s or Δ*R* greater than 2–3 km (Figs. 12 and 13, and the far Δ*R* group in Fig. 9). To conclude, the scaling of damping indicated that the features, such as local site effects in the shallow subsurface layer, were more easily subjected to higher damping due to soil nonlinearity, and lower damping occurred at higher frequencies. Furthermore, lower damping for high frequencies might first disobey the de-amplification in high frequencies in soil nonlinearity observations; however, damping would respond in each oscillatory cycle as higher frequency means more cycling, which consequently reduce high-frequency energy. In this study, we therefore provide a different way to check the frequency-dependent *Q*, *h* and the proportional trend of damping-strain relations for multiple layered structures from seismic observation directly that would close to true local site response during strong motion earthquakes, and would prevent some insufficient from tri-axial test experiment while core samples were not experiment on-site and might be decompressed back to laboratory. We might have some more evidences to re-evaluate the frequency-dependent damping-strain relations if we can have a more densely seismic array such as space interval smaller than maybe 100 m and recorded a series of weak to strong motions in the near future since the limitation of the existing seismic records in SMART1.

## 4. Conclusions

In this study, a frequency-dependent damping *h(f)* was calculated from a frequency-dependent *Q(f)* through the spectral ratio method using SMART1 records. Each *Q(f)* was belong to topmost subsurface layer with a thickness equal to Δ*R* and has a mean trend of $15f^{0.9}$ and a confident range from $5f^{0.9}$ to $45f^{0.9}$ in the near-surface structures in the SMART1 region (Fig. 6). First, clear soil nonlinearity trends were checked in the SMART1 database considering the stress-strain relation and DNL calculation (Fig. 7) to ensure that a clear feature could be identified in the following procedures. A strain-dependent damping in a short Δ*R* indicated a proportional trend in the frequency range from 2 Hz to 8 Hz, which would mainly be controlled from the site effect in the near-surface layers, and a 40%–50% increase in *h(f)* was identified from the strain proxy 0.01%–0.1% (Fig. 9). Furthermore, an independent correlation between the damping ratio and source effect was found from the source scaling (Fig. 10), but not much dependency occurred in the near field while $R_{hypo}$ was greater than 70 km in the distance scaling relation (Fig. 11). Owing to the spectral ratio of the differences in seismic ray paths, the deeper structure, deeper path, and higher *Q* induced a lower damping ratio response in the far-field records. Finally, the site effect was found to mostly influence damping in the softer and shallow subsurface sedimentary layers. The strong motions observed by the dense SMART1 allow us to measure the damping ratio variation of sedimentary layers in different frequencies and intensities. In particular, a mean Vs below 600 m/s and ΔR smaller than 500 m showed larger damping in the frequency band from 3 Hz to 8 Hz (Figs. 12 and 13), which corresponds to the underground structures of Vs less than 1 km/s from the MHVSR measurements.

## Author statement

C.H. Kuo: Writing – original draft, Methodology, Validation. J.Y.

Huang: Writing – review & editing, Software, Formal analysis, Supervision. C.M. Lin: Data curation, Visualization. C.T. Chen: Investigation, Resources. K.L. Wen: Conceptualization, Resources.

## Declaration of competing interest

The authors declare that they have no known competing financial interests or personal relationships that could have appeared to influence the work reported in this paper.

## Acknowledgements

We would like to thank the Institute of Earth Sciences (IES), Academia Sinica of Taiwan for providing the seismic data of SMART1. The Ministry of Science and Technology, R.O.C. supported this paper through grants MOST 108-2116-M-492-005 and MOST 108-2116-M-492-006.

## References

[1] Aguirre J, Irikura K. Nonlinearity, liquefaction, and velocity variation of soft soil layers in Port Island, Kobe, during the Hyogo-ken Nanbu earthquake. Bull Seismol Soc Am 1997;87(5):1244–58.
[2] Boore DM, Seekins L, Joyner WB. Peak acceleration from the 17 october 1989 loma Prieta earthquake. Seismol Res Lett 1989;60:151–66.
[3] Darragh RB, Shakal AF. The site response of two rock and soil station pairs to strong and weak ground motion. Bull Seismol Soc Am 1991;81:1885–99.
[4] Wen KL, Chang TM, Lin CM, Chiang HJ. Identification of nonlinear site response using the H/V spectral ratio method. Terr Atmos Ocean 2006;17(3):533–46.
[5] Borcherdt RD. Effects of local geology on ground motion near San Francisco Bay. Bull Seismol Soc Am 1970;60(1):29–61.
[6] Boore DM. Stochastic simulation of high-frequency ground motions based on seismological models of the radiated spectra. Bull Seismol Soc Am 1983;73(6):1865–94.
[7] Chin BH, Aki K. Simultaneous study of the source, path, and site effects on strong ground motion during the 1989 Loma Prieta earthquake: a preliminary result on pervasive nonlinear site effects. Bull Seismol Soc Am 1991;81(5):1859–84.
[8] Tucker BE, King JL. Dependence of sediment-filled valley response on input amplitude and valley properties. Bull Seismol Soc Am 1984;74:153–65.
[9] Nakamura Y. A method for dynamic characteristies estimation of subsurface using microtremor on the ground surface. QR of RTRI 1989;30(1):25–33.
[10] Nakamura Y. What is the Nakamura method? Seismol Res Lett 2019;90(4):1437–43.
[11] Jarpe SP, Hutchings LJ, Hauk TF, Shakal AF. Selected strong and weak-motion data from the Loma Prieta Earthquake sequence. Seismol Res Lett 1989;60(4):167–76.
[12] Boore DM. Simulation of ground motion using the stochastic method. Pure Appl Geophys 2003;160:635–76.
[13] Aki K. Local site effects on weak and strong ground motion. Tectonophysics 1993;218(1–3):93–111.
[14] Bolt BA, Tsai YB, Yeh K, Hsu MK. Earthquake strong ground motion recorded by a large near-source array of digital seismographs. Earthq Eng Struct Dynam 1982;10:561–73.
[15] Chiu HC, Yeh YT, Ni SD, Lee L, Liu WS, Wen CF, Liu CC. A new strong-motion array in Taiwan: SMART-2. Terr Atmos Ocean 1994;5:463–75.
[16] Shin TC, Tsai YB, Yeh YT, Liu CC, Wu YM. Strong-motion instrumentation programs in Taiwan. in Handbook of earthquake and engineering seismology 2003, W. H. K. Lee, H. Kanamori and P. C. Jennings (Editors), Academic Press, New York, 1057-1602.
[17] Tsai YB, Lee CP. Strong motion instrumentation programs in taiwan- past and present. NATO Science Series 2005;58:255–78.
[18] Beresnev IA, Wen KL, Yeh YT. Source, path, and site effects on dominant frequency and spatial variation of strong ground motion recorded by SMART1 and SMART2 arrays in Taiwan. Earthq Eng Struct Dynam 1994;23:583–97.
[19] Beresnev IA, Wen KL, Yeh YT. Nonlinear soil amplification: its corroboration in Taiwan. Bull Seismol Soc Am 1995;85:496–515.
[20] Beresnev IA, Wen KL, Yeh YT. Seismological evidence for nonlinear elastic ground behavior during large earthquakes. Soil Dynam Earthq Eng 1995;14:103–14.
[21] Beresnev IA, Wen KL. Nonlinear ground response - a reality? (A review). Bull Seismol Soc Am 1996;86(6):1964–78.
[22] Wen KL. Non-linear soil response in ground motions. Earthq Eng Struct Dynam 1994;23(6):599–608.
[23] Wen KL, Beresnev IA, Yeh YT. Nonlinear soil amplification inferred from downhole strong seismic motion data. Geophys Res Lett 1994;21:2625–8.
[24] Wen KL, Beresnev IA, Yeh YT. Investigation of nonlinear site amplification at two downhole strong ground motion arrays in Taiwan. Earthq Eng Struct Dynam 1995;24:313–24.
[25] Maeda T, Sasatani T. Strong ground motions from an Mj 6.1 inland crustal earthquake in Hokkaido, Japan: the 2004 Rumoi earthquake. Earth Planets Space 2009;61:689–701.
[26] Wen KL, Huang JY, Li XJ, Zhou ZH, Wen RZ. Nonlinear site response of the 2008 Wenchuan, China earthquake from time-frequency analysis. Proc. 8CUEE. 2011a. P121, Tokyo, Japan.
[27] Wen KL, Huang JY, Chen CT, Cheng YW. Nonlinear site response of the 2010 Dar field, New Zealand earthquake sequence. In: Proc. Esg4; 2011. P1-8, Santa Barbara, USA.
[28] Dhakal YP, Kubo H, Suzuki W, Kunugi T, Aoi S, Fujiwara H. Analysis of strong ground motions and site effects at Kantipath, Kathmandu, from 2015 Mw 7.8 Gorkha, Nepal, earthquake and its aftershocks. Earth Planets Space 2016;68:58.
[29] Rong MS, Wang ZM, Woolery EW, Lyu YJ, Li XJ, Li SY. Nonlinear site response from the strong ground-motion recordings in western China. Soil Dynam Earthq Eng 2016;82:99–110.
[30] Chen CT, Chang SC, Wen KL. Stochastic ground motion simulation of the 2016 Meinong, Taiwan earthquake. Earth Planets Space 2017;69:62.
[31] Dhakal YP, Aoi S, Kunugi T, Suzuki W, Kimura T. Assessment of nonlinear site response at ocean bottom seismograph sites based on S-wave horizontal-to-vertical spectral ratios: a study at the Sagami Bay area K-NET sites in Japan. Earth Planets Space 2017;69:29.
[32] Dhakal YP, Kunugi T, Kimura T, Suzuki W, Aoi S. Peak ground motions and characteristics of nonlinear site response during the 2018 Mw 6.6 Hokkaido eastern Iburi earthquake. Earth Planets Space 2019;71:56.
[33] Huang JY, Zaalishvili VB, Melkov DA, Kuo CH, Wen KL, Chen CT. Progress of soil nonlinearity researches of recent years in Russia and Taiwan. Geology and Geophysics of Russian South 2020;10(2):95–112.
[34] Noguchi S, Sasatani T. Quantification of degree of nonlinear site response. In: Proc. 14WCEE; 2008. P1-8, Beijing, China.
[35] Noguchi S, Sasatani T. Nonlinear soil response and its effects on strong ground motions during the 2003 Miyagi-Oki intraslab earthquake. Earthquake 2011;63(2):165–87 [in Japanese)].
[36] Regnier J, Cadet H, Bonilla LF, Bertrand E, Semblat JF. Assessing nonlinear behavior of soils in seismic site response: statistical analysis on KiK-net strong-motion data. Bull Seismol Soc Am 2013;103(3):1750–70.
[37] Ren YF, Wen RZ, Yao XX, Ji K. Five parameters for the evaluation of the soil nonlinearity during the Ms8.0 Wenchuan Earthquake using the HVSR method. Earth Planets Space 2017;69:116.
[38] Kubo H, Nakamura T, Suzuki W, Dhakal YP, Kimura T, Kunugi T, Aoi S. Ground motion characteristics and nonlinear soil response observed by DONET1 seafloor observation network during the 2016 Southeast Off-Mie, Japan, earthquake. Bull Seismol Soc Am 2019;109(3):976–86.
[39] Ji K, Wen RZ, Ren YF, Dhakal YP. Nonlinear seismic site response classification using K-means clustering algorithm: case study of the September 6, 2018 Mw6.6 Hokkaido Iburi-Tobu earthquake, Japan. Soil Dynam Earthq Eng 2020;128:105907.
[40] Zhou Y, Wang HW, Wen RZ, Ren YF, Ji K. Insights on nonlinear soil behavior and its variation with time at strong-motion stations during the Mw7.8 Kaikōura, New Zealand earthquake. Soil Dynam Earthq Eng 2020;136:106215.
[41] Duncan JM, Chang CY. Nonlinear analysis of stress and strain in soils. J Soil Mech Found Div 1970;96(5):1629–53.
[42] Hardin BO, Drnevich VP. Shear modulus and damping in soils: measurement and parameter effects. J Soil Mech Found Div 1972;98(6):603–24.
[43] Finn WDL, Lee KW, Martin GR. An effective stress model for liquefaction. J Geotech Engng Div, ASCE 1977;103(GT6):517–33.
[44] Mohammadioun B, Pecker A. Low-frequency transfer of seismic energy by superficial soil deposits and soft rocks. Earthq Eng Struct Dynam 1984;12:537–64.
[45] Pavlenko OV, Irikura K. Estimation of nonlinear time-dependent soil behavior in strong ground motion based on vertical array data. Pure Appl Geophys 2003;160:2365–79.
[46] Pavlenko OV, Irikura K. Identification of the nonlinear behavior of liquefied and non-liquefied soils during the 1995 Kobe earthquake. Geophys J Int 2005;160:539–53.
[47] Pavlenko OV, Loh CH. Nonlinear identification of the soil response at Dahan downhole array site during the 1999 Chi-Chi earthquake. Soil Dynam Earthq Eng 2005;25:241–50.
[48] Pavlenko OV, Irikura K. Nonlinear behavior of soils revealed from the records of the 2000 Tottori, Japan, Earthquake at stations of the digital strong-motion network Kik-Net. Bull Seismol Soc Am 2006;96(6):2131–45.
[49] Pavlenko OV, Wen KL. Estimation of nonlinear soil behavior during the 1999 chi-chi, taiwan, earthquake. Pure Appl Geophys 2008;165:373–407.
[50] Idriss IM. Use of $V_{S30}$ to represent local site condition. In: Proc. Esg4; 2011. P1-63, Santa Barbara, USA.
[51] Chandra J, Guéguen P, Steidl JH, Bonilla LF. In situ assessment of the G–γ curve for characterizing the nonlinear response of soil: application to the Garner valley downhole array and the wildlife liquefaction array. Bull Seismol Soc Am 2015;105(2A):993–1010.
[52] Chandra J, Guéguen P, Bonilla LF. PGA-PGV/Vs considered as a stress–strain proxy for predicting nonlinear soil response. Soil Dynam Earthq Eng 2016;85:146–60.
[53] Guéguen P. Predicting nonlinear site response using spectral acceleration vs PGV/Vs30: a case history using the Volvi-test site. Pure Appl Geophys 2016;173:2047–63.

[54] Derras B, Bard PY, Cotton F. $V_{S30}$, slope, $H_{800}$ and $f_0$: performance of various site-condition proxies in reducing ground-motion aleatory variability and predicting nonlinear site response. Earth Planets Space 2017;69:133.

[55] Eskandarinejad A, Jahanandish M, Zafarani H. Divergence between nonlinear and equivalent-linear 1D site response analyses for different VS realizations of typical clay sites. Pure Appl Geophys 2017;174:3955–78.

[56] Viens L, Denolle MA, Hirata N, Nakagawa S. Complex near-surface rheology inferred from the response of greater Tokyo to strong ground motions. J Geophys Res Solid Earth 2018;123:5710–29.

[57] Guéguen P, Bonilla LF, Douglas J. Comparison of soil nonlinearity (In situ stress-strain relation and G=Gmax reduction) observed in strong-motion databases and modeled in ground-motion prediction equations. Bull Seismol Soc Am 2019;109(1):178–86.

[58] Kuo CH, Huang JY, Lin CM, Hsu TY, Chao SH, Wen KL. Strong ground motion and pulse-like velocity observations in the near-fault region of the 2018 Mw 6.4 Hualien, Taiwan, earthquake. Seismol Res Lett 2019;90(1):40–50.

[59] Derras B, Bard PY, Régnier J, Cadet H. Non-linear modulation of site response: sensitivity to various surface ground-motion intensity measures and site-condition proxies using a neural network approach. Eng Geol 2020;269:105500.

[60] Xu B, Rathje EM, Hashash Y, Stewart J, Campbell K, Silva WJ. $\kappa_0$ for soil sites: observations from Kik-net sites and their use in constraining small-strain damping profiles for site response analysis. Earthq Spectra 2020;36(1):111–37.

[61] Tao Y, Rathje E. Taxonomy for evaluating the site-specific applicability of one-dimensional ground response analysis. Soil Dynam Earthq Eng 2020;128:105865.

[62] Shi J, Asimaki D. On the applicability of shear strain index as a proxy for site response nonlinearity. Proc. of Geotechnical Earthquake Engineering and Soil Dynamics V GSP 2018;291:550–8. June 10-13, Austin, Texas. ISBN (PDF): 9780784481462.

[63] Peng HY, Wen KL. Downhole instrument orientations and near surface Q analysis from the SMART2 array data. Terr Atmos Ocean 1993;4:367–80.

[64] Chang LS, Yeh YT. The Q value of strong ground motions in Taiwan. Bull Inst Earth Sci Acad Sin 1983;3:127–48.

[65] Chen KC, Shin TC, Wang JH. Estimates of coda Q in taiwan. Proc Geol Soc China 1989;32:339–53.

[66] Wang JH, Liu KS. Azimuthal variation of code Q in northern Taiwan. Geophys Res Lett 1990;17:1315–8.

[67] Wang JH. Q value of Taiwan: a review. J Geol Soc China 1993;36(1):15–24.

[68] Chung JK, Chen YL, Shin TC. Spatial distribution of coda Q estimated from local earthquakes in Taiwan area. Earth Planets Space 2009;61:1077–88.

[69] Iwata T, Irikura K. Source parameters of the 1983 Japan sea earthquake sequence. J Phys Earth 1988;36:155–84.

[70] Parolai S, Bindi D, Augliera P. Application of the generalized inversion technique (GIT) to a microzonation study: numerical simulations and comparison with different site-estimation techniques. Bull Seismol Soc Am 2000;90(2):286–97.

[71] Oth A, Bindi D, Parolai S, Wenzel F. S-wave attenuation characteristics beneath the Vrancea region in Romania: new insights from the inversion of ground-motion spectra. Bull Seismol Soc Am 2008;98:2482–97.

[72] Zafarani H, Hassani B, Ansari A. Estimation of earthquake parameters in the Alborz seismic zone, Iran using generalized inversion method. Soil Dynam Earthq Eng 2012;42:197–218.

[73] Grendas I, Theodoulidis N, Hatzidimitriou P, Margaris B, Drouet S. Determination of source, path and site parameters based on nonlinear inversion of accelerometric data in Greece. Bull Earthq Eng 2018;16:5061–94.

[74] Wang HW, Ren YF, Wen RZ. Source parameters, path attenuation and site effects from strong-motion recordings of the Wenchuan aftershocks (2008-2013) using a non-parametric generalized inversion technique. Geophys J Int 2018;212:872–90.

[75] Sokolov V, Loh CH, Wen KL. Empirical model for estimating Fourier amplitude spectra of ground acceleration in Taiwan region. Earthq Eng Struct Dynam 2000;29:339–57.

[76] Sokolov V, Loh CH, Wen KL. Site-dependent design input ground motion estimations for the Taipei area: a probabilistic approach. Probabilist Eng Mech 2001;16:177–91.

[77] Roumelioti Z, Beresnev IA. Stochastic finite-fault modeling of ground motions from the 1999 Chi-Chi, Taiwan, earthquake: application to rock and soil sites with implications for nonlinear site response. Bull Seismol Soc Am 2003;93(4):1691–702.

[78] Sokolov V, Wen KL, Miksat J, Wenzel F, Chen CT. Analysis of Taipei basin response for earthquakes of various depths and locations using empirical data. Terr Atmos Ocean 2009;20(5):687–702.

[79] Chung JK. Peak ground motion predictions with empirical site factors using Taiwan Strong Motion Network recordings. Earth Planets Space 2013;65:957–72.

[80] Huang JY, Wen KL, Lin CM, Kuo CH, Chen CT, Chang SC. Site correction of a high-frequency strong-ground-motion simulation based on an empirical transfer function. J Asian Earth Sci 2017;138:399–415.

[81] Gurevich B, Pevzner R. How frequency dependency of Q affects spectral ratio estimates. Geophysics 2015;80(2):A39–44.

[82] Wang YJ, Ma KF, Mouthereau F, Eberhart-Phillips D. Three-dimensional Qp- and Qs-tomography beneath Taiwan orogenic belt: implications for tectonic and thermal structure. Geophys J Int 2010;180:891–910.

[83] Wang YJ, Lin YY, Lee MC, Ma KF. Fault zone Q values derived from Taiwan Chelungpu Fault borehole seismometers (TCDPBHS). Tectonophysics 2012;578:76–86.

[84] Wang ZW, Zhao DP, Liu X, Li XB. Seismic attenuation tomography of the source zone of the 2016 Kumamoto earthquake (M 7.3). J Geophys Res Solid Earth 2017;122:1–20.

[85] Idriss IM, Sun J. User's manual for SHAKE91: a computer program for conducting equivalent linear seismic response analyses of horizontally layered soil deposits. 1993.

[86] Lee CP, Tsai YB, Wen KL. Analysis of nonlinear site response using the LSST downhole accelerometer array data. Soil Dynam Earthq Eng 2006;26(5):435–60.

[87] Zalachoris G, Rathje EM. Evaluation of one-dimensional site response techniques using borehole arrays. J Geotech Geoenviron Eng 2015;141(12):04015053.

[88] Kaklamanos J, Bradley BA, Thompson EM, Baise LG. Critical parameters affecting bias and variability in site-response analyses using KiK-net downhole array data. Bull Seismol Soc Am 2013;103(3):1733–49.

[89] Gibbs JF, Boore DM, Joyner WB, Fumal TE. The attenuation of seismic shear waves in Quaternary alluvium in Santa Clara Valley, California. Bull Seismol Soc Am 1994;84:76–90.

[90] Boore DM, Gibbs JF, Joyner WB. Damping values derived from surface-source, downhole-receiver measurements at 22 sites in the San Francisco bay area of central California and the San Fernando valley of southern California. Bull Seismol Soc Am 2020. https://doi.org/10.1785/0120200225.

[91] Assimaki D, Kausel E. An equivalent linear algorithm with frequency-and pressure- dependent moduli and damping for the seismic analysis of deep sites. Soil Dynam Earthq Eng 2002;22(9–12):959–65.

[92] Kausel E, Assimaki D. Seismic simulation of inelastic soils via frequency-dependent moduli and damping. J Eng Mech 2002;128(1):34–47.

[93] Huang DR, Wang G, Wang CY, Jin F. A modified frequency-dependent equivalent linear method for seismic site response analyses and model validation using KiK-net borehole arrays. J Earthq Eng 2020;24(5):827–44.

[94] Aki K. Attenuation of shear-waves in the lithosphere for frequency from 0.5 to 25 Hz. Phys Earth Planet In 1980;21:50–60.

[95] Console R, Rovelli A. Attenuation parameters for Friuli region from strong-motion accelerogram spectra. Bull Seismol Soc Am 1981;71(6):1981–91.

[96] Konno K, Ohmachi T. Ground-motion characteristics estimated from spectral ratio between horizontal and vertical components of microtremor. Bull Seismol Soc Am 1998;88(1):228–41.

[97] Kottke A, Abrahamson NA, Boore DM, Bozorgnia Y, Goulet C, Hollenback J, Kishida T, Kiureghian AD, Ktenidou OJ, Kuehn N, Rathje EM, Silva WJ, Thompson E, Wang X. Selection of random vibration procedures for the NGA-East project. PEER report 2018. 2018/05:1-60.

[98] Um J, Thurber C. A fast algorithm for two-point seismic ray tracing. Bull Seismol Soc Am 1987;77(3):972–86.

[99] Koketsu K, Sekine S. Pseudo-bending method for three-dimensional seismic ray tracing in a spherical earth with discontinuities. Geophys J Int 1998;132:339–46.

[100] Tsai CY. The rapid travel-time sequence method for earthquake locating and application of the local earthquake early warning arrays in Taiwan. master thesis of National Cheng-Kung University; 2015pp182 [in Chinese with English abstract)].

[101] Chen YL, Shin TC. Study on the earthquake location of 3-d velocity structure in the taiwan area. Meteorological Bulletin 1998;42(2):135–69 [in Chinese with English abstract)].

[102] Sánchez-Sesma FJ, Rodríguez M, Iturrarán-Viveros U, Luzón F, Campillo M, Margerin L, García-Jerez A, Suarez M, Santoyo MA, Rodríguez-Castellanos A. A theory for microtremor H/V spectral ratio: application for a layered medium. Geophys J Int 2011;186:221–5.

[103] García-Jerez A, Luzón F, Sánchez-Sesma FJ, Lunedei E, Albarello D, Santoyo MA, Almendros J. Diffuse elastic wavefield within a simple crustal model. Some consequences for low and high frequencies. J Geophys Res Solid Earth 2013;118(10):5577–95.

[104] Chen CT, Kuo CH, Lin CM, Huang JY, Wen KL. Evaluation of shallow shear wave velocity using microtremors. Proc. 15NCSE&5NCEE. 2020;1–7:133 [Tainan, Taiwan. (in Chinese with English abstract)].

[105] Wen KL, Huang JY. Dense microtremor survey for site effect study in Taiwan. In: Proc. 15WCEE; 2012. P1-8, Lisbon, Portugal.

[106] Kuo CH, Wen KL, Lin CM, Wen S, Huang JY. Investigating near surface S-wave velocity properties using ambient noise in southwestern Taiwan. Terr Atmos Ocean 2015;26(2):205–11.

[107] Kuo CH, Chen CT, Lin CM, Wen KL, Huang JY, Chang SC. S-wave velocity structure and site effect parameters derived by microtremor arrays in the Western Plain of Taiwan. J Asian Earth Sci 2016;128:27–41.

[108] Sun J, Hutchinson T, Clahan K, Menq F, Lo E, Chang WJ, Tsai CC, Ma KF. Geotechnical reconnaissance of the 2016 Mw 6.3 meinong earthquake, taiwan. GEER Association Report; 2016. https://doi.org/10.18118/G6PK5J. GEER-046.

[109] Huang JY, Kuo CH, Lin CM, Hsieh HH, Wen KL. Construction and application of site databases in Taiwan after 1999 ChiChi Taiwan earthquake. In: Proc. 7ACEE2018; 2018. ACEE0142, P1-8, Bangkok, Thailand.

[110] Huang JY, Wen KL, Lin CM, Kuo CH. Rapid site effect evaluation for recent disaster earthquakes in Taiwan from dense microtremor H/V measurements. In: Proc. CHICHI20; 2019. P1-7, Taipei, Taiwan.

[111] Chao SH, Lin CM, Kuo CH, Huang JY, Wen KL, Chen YH. Implementing horizontal-to-vertical Fourier spectral ratios and spatial correlation in a ground-motion prediction equation to predict site effects. Earthq Spectra 2020;37(2):827–56.

[112] Aki K. Scaling law of seismic spectrum. J Geophys Res 1967;72(4):1217–31.

[113] Brune JN. Tectonic stress and the spectra of seismic shear waves from earthquake. J Geophys Res 1970;75(26):4997–5009.

[114] Chen KC, Huang WG, Wang JH. Relationships among magnitudes and seismic moment of earthquakes in the Taiwan region. Terr Atmos Ocean 2007;18(5):951–73.

[115] Abrahamson NA. Estimation of seismic wave coherency and rupture velocity using the SMART-1 strong motion array recordings. Berkeley: Report of University of California; 1985. UCB/EERC-85/2.
[116] Shieh CF. Estimation of Q value by SP/S spectral ratio. Terr Atmos Ocean 1992;3 (4):469–82.
[117] Ayyub BM, Mccuen RH. Probability, statistics, and reliability for engineers and scientists. second ed. Washington, D.C.: A CRC Press Company; 2003.
[118] Electric Power Research Institute (Epri). Guidelines for determining design basis ground motions. EPRI: Final Report; 1993. TR-102293.